Design Workflow of a Symmetric Traveling Wave Antenna for Fast Ion Production on DD Tokamaks

J. G. van de Lindt[a], S. J. Wukitch[a], N. Bertelli[b], S. Shiraiwa[b]

[a]**Plasma Science and Fusion Center, Massachusetts Institute of Technology, Cambridge, MA 02139, USA** [b]**Princeton Plasma Physics Laboratory, 100 Stellarator Rd, Princeton, NJ 08540, USA**

Abstract

Initial computational plasma physics scoping and a finite element method (FEM) antenna modeling design workflow for a symmetric center-fed high-field side (HFS) high harmonic fast wave traveling wave array (TWA) antenna are reported here. The TWA is designed to generate a test population of fast deuterium ions in an existing D-D tokamak by heating neutral beam deuterium ions, accelerating them from 80 keV to several hundred keV. The resulting fast particles are tailored to mimic key reactor energetic particle parameters with regards to exciting Alfven Eigenmode (AE) instabilities, allowing for a D-D tokamak like DIII-D or ASDEX-U to replicate reactor-relevant conditions experimentally. Initial scenario scoping for high single-pass absorption (SPA) as well as good preferential fast ion damping relative to electron damping was completed using the ray-tracing/Fokker-Planck codes GENRAY and CQL3D. Python RF network analysis packages were used to create a custom TWA optimization tool to inform a COMSOL flat antenna design, and Petra-M was used to study cold plasma effects. The TWA produced by this workflow has several novel features when compared to previous TWA studies, including symmetric center feeding, and passive end straps for image current cancellation for reduced impurity production. We show here that the antenna design workflow can readily produce TWA antennas optimized for reflection coefficient, image current cancellation, and launched power spectrum shape; and that a population of fast ions can be generated in the correct region of parameter space, warranting future more detailed studies.

---

1 Introduction

To prepare for burning plasma experiments and reactor power plants that have large populations of fast fusion alphas and large RF and neutral beam heating/current drive power, further experimental validation of energetic particle theory and modeling is required. Devices like ITER [1] and SPARC [2] will be able to validate fast particle predictions directly in the burning plasma regime; however, ITER is still many years from D-T operation and SPARC is a privately owned device. An alternative to using burning experiments to study fast particles is to quickly build up experimental capability for fast particle creation on existing D-D devices. In such an experiment, key energetic particle (EP) parameters would need to closely replicate those of a burning device. In this work, a center-fed high field side (HFS) traveling wave array (TWA) antenna that features image current cancellation is introduced for channeling power to neutral beam ions to create reactor-relevant EP populations. This paper first introduces the importance of energetic particles, the physics of high harmonic fast wave damping, the computational tools used to scope initial plasma physics objectives, and the antenna design tools. The results of the plasma physics scoping and the methodology for antenna design are explained, followed by an initial antenna design point

and next steps. Although the TWA here is designed for the specific application of EP generation, choices are made, where possible, so that lessons learned from the TWA here are also relevant to antenna design for bulk heating in a future reactor device, as several studies point to the TWA antenna as an attractive solution for that application [3].

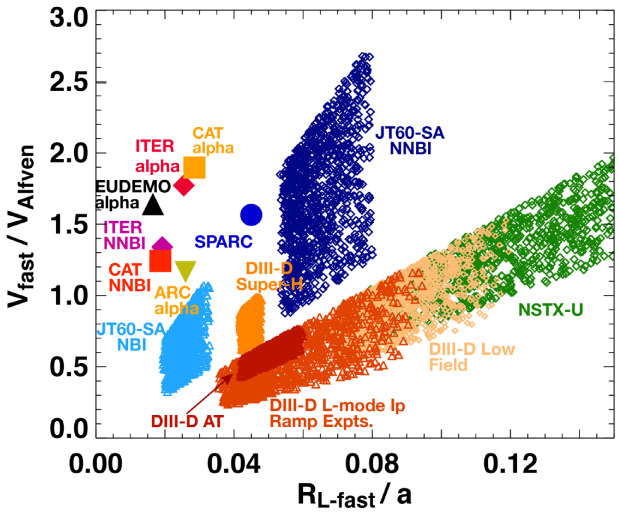

Figure 1: Representative energetic particle parameter space of various tokamaks, plotted with the ratio of fast particle velocity to Alfven velocity on the y-axis and fast particle Larmor radius to device minor radius on the x-axis. Modified from [4]

1.1 The Role of Energetic Particles

For economical fusion devices, alpha particles must be able to deposit their energy in the thermal bulk before being lost to maintain the burning plasma and avoid potentially catastrophic damage to the plasma-facing components [5]. These fast particles experience enhanced curvature and $\nabla \mathbf{B}$ drifts, which are proportional to the particle energy [6]. As a result, EP's tend to drift off of magnetic flux surfaces. Cyclic aspects of the EP orbit, such as cyclotron motion, mirror bouncing, and toroidal precession, can resonate with electric and magnetic field perturbations in the machine. These resonances can alter the orbital motion of the particle, which can result in large transport step sizes as topological barriers in invariant space are crossed. Large transport step sizes can result in much lower particle confinement time for the fast particles and direct loss to the device wall [6].

In tokamak reactors, three major types of perturbations are important when considering their interaction with EP's. The first two are normal modes of the background plasma: counterpropagating toroidal Alfven eigenmodes (TEA), and reversed shear Alfven eigenmodes (RSAE) [5]. The third type, energetic particle modes (EPM), become important when the EP beta, β_{EP}, is comparable to the thermal plasma beta, β_{th} [5].

Four major EP features that would need to be replicated are the EP velocity relative to the Alfven velocity ($V_{\mathrm{fast}}/V_{\mathrm{A}}$), the fast particle beta relative to the thermal beta ($\beta_{\mathrm{EP}}/\beta_{\mathrm{th}}$), the finite orbit width of the EP relative to the device minor radius ($\rho_{\mathrm{L,EP}}/a$ or $R_{\mathrm{bananna,EP}}/a$), as well as the distribution function [5]. Figure 1 shows where devices fall with respect to $V_{\mathrm{fast}}/V_{\mathrm{A}}$ and $\rho_{\mathrm{L,EP}}/a$. For completed experimental campaign achievements, a scatter of points is shown. For the single-point devices, these are the projected future operating points of machines that have not yet been completed, including SPARC [2], ARC [7], ITER [1], and EU-DEMO [8]. Generally, high fields and large machines will cause the Larmor radius over the minor radius $\rho_{\mathrm{L,EP}}/a$ to be small. Lower fields, higher densities, or very hot or fast ions will cause $V_{\mathrm{fast}}/V_{\mathrm{A}}$ to be large. It is for these reasons that it can be difficult for a smaller cooler machine with lower fields to match both $\rho_{\mathrm{L,EP}}/a$ and $V_{\mathrm{fast}}/V_{\mathrm{A}}$ on either a larger device (ITER, DEMO), or a higher field device (SPARC, ARC).

1.2 High Harmonic Fast Wave Physics

High harmonic fast waves (HHFW) with frequencies above 20× the bulk ion cyclotron frequency were explored theoretically by Ono [9] for localized electron heating and current drive in high beta plasmas, and were experimentally investigated with deuterium cyclotron harmonics in the range of 5 to 12 on NSTX (similar to the 5 to 9 range used in this work) for comparing the power channeled to NBI ions and to

electrons [10] [11]. Extensive modeling work for the NSTX-U [12] HHFW system was investigated to understand the influence of NBI damping and the competition between it and electron damping [13], as well as for how power partitioning between ions and electrons is effected by launched $n_{||}$ [13].

Many existing D-D experiments have neutral beam systems that can generate deuterium ions with energies in the 10s of keV's, with DIII-D's beam system capable of generating 80 keV ions [14]. These fast deuterium ions can readily be damped on via high harmonic fast waves (with harmonic numbers in the range of 4 to 8) due to cyclotron damping being stronger at a given harmonic for large $k_\perp \rho_L$, where $k_\perp$ is the perpendicular wave number and ρ_L is the EP Larmor radius. Cyclotron damping is given by Stix [15] in Equation 1 as an increase in the particle perpendicular energy, $W_\perp$:

$$\frac{dW_\perp}{dt} = qE\Omega_c\rho_L \times \mathrm{Re}\left[\sum_{n=-\infty}^{\infty} J_n(k_\perp\rho_L)e^{in(\Omega_c t+\phi)-i\omega_{\mathrm{RF}}\phi}\right]\mathrm{Re}[e^{i(\Omega_c t+\phi)}], \quad (1)$$

whenever a particle satisfies the Doppler-shifted wave-particle resonant condition [14] given by $\omega_{\mathrm{RF}} = k_{||}v_{||} + n\Omega_c$. Here, q is the particle charge, E is the electric field magnitude, Ω_c is the cyclotron frequency, and ω_{RF} is the launched frequency. Thus, RF power launched at frequencies corresponding to harmonics of the cyclotron frequency will channel power directly to the 80 keV beam deuterons which have larger $k_\perp\rho_L$, and not to the slower thermal bulk deuterons, producing a population of energetic RF tail ions.

Two key physics questions for a high harmonic fast wave system designed to heat NBI ions are: how readily can RF power be channeled to the beam ions while not to the bulk electrons, and how can strong single-pass absorption (SPA) be achieved? The former is required for the main design goal of producing a population of energetic particles with reactor-relevant parameters, as shown in Figure 1, while the latter is desired because good SPA avoids deleterious losses of power at the far scrape-off layer, as well as reflected power passing through undesired portions of the discharge.

To scope the beam power, RF power, and antenna $n_{||}$ required to meet the design goals of good SPA and selectivity for ion damping over electron damping, the GENRAY [16] ray-tracing code coupled to the CQL3D [17] Fokker-Planck code were used at a design frequency of 96 MHz, targeting the 8th harmonic near the center of the plasma. The choice of 8th harmonic is explained in Section 2. Included with CQL3D is Freya, which is a neutral beam solver. Freya realistically injects NB particles and tracks them until ionization occurs, which is then a source term for ions and electrons in the Fokker-Planck equation that CQL3D solves. The two major limitations here are that GENRAY uses the ray approximation, and CQL3D assumes zero-banana width. These limitations are addressed later in the Discussion and Limitations section. The use of GENRAY/CQL3D in this work is limited to scoping NBI power, $n_{||}$, and RF power, and selecting for good SPA and ion channeling only.

1.3 Traveling Wave Array Antenna

To launch the ∼8th harmonic 96 MHz fast wave, a traveling wave array (TWA) antenna was selected due to its numerous advantages over traditional strap antennas and the need for more experimental experience with this antenna configuration given its relevance to reactor ICRH applications [3]. The TWA is a series of inductively coupled straps aligned perpendicular to the field lines with capacitors shorting the top of each strap to the antenna box, an example is shown in Figure 2 (a). In a traditional TWA comb-line antenna, all but the first strap are passive structures.

Traveling wave array antennas have been studied extensively for plasma RF heating and current drive applications. Chiu in 1984 studied the TWA for current-drive applications [18], and Pinsker proposed comb-line array antennas as a promising option for launching fast waves with adjustable $n_{||}$ in 1994 [19]. Ragona and

Messiaen in a series of works have looked at designing TWA antennas for ion cyclotron resonance heating (ICRH) on WEST [20] [21], and future machines like ITER and DEMO [22] [23], as well as having built up large-scale mock-ups on the TITAN test facility [24] [25]. Ongena looked at both ICRH and ion cyclotron current drive (ICCD) with TWA antennas at the T-15MD Tokamak [26]. Finally, the helicon TWA antenna at very high cyclotron harmonics was explored for current drive applications theoretically by Prater [27] and experimentally by Pinsker [28] at DIII-D.

Typically, a TWA antenna is fed by one coaxial port on one of the end straps, and power is removed from the other side by a second coaxial port. If the per-strap plasma loading is less than the mutual coupling to the next strap, then the structure is expected to be more resilient to changes in the plasma load than traditional ICRH antennas [23]. Load resiliency of TWAs may remove or mitigate the need for active impedance matching systems. In addition to good load resiliency, TWAs typically have more selective $P(n_{||})$ power spectra than traditional ICRF antennas, which is desirable for meeting the plasma physics goals of an antenna. This higher selectivity is due to the higher number of straps on a TWA, which is possible because increased coaxial feeding is not required for increased strap number. For reactor applications, being able to operate with only two coaxial feeds while being able to change the number of straps is an advantage because any cuts through the breeder blanket lead to a reduced tritium breeding ratio and increased avenues for neutron streaming. More straps also come with the added benefit of reducing the power density and voltage of the antenna [20].

In this work, the comb-line TWA in Figure 2 (a) is modified to address the need for a symmetric $P(n_{||})$ power spectrum and reduced impurity production. A symmetric power spectrum is desired so that ideally the antenna can damp on a zero-torque co/counter neutral beam configuration [29] in which two beams are used at opposite toroidal injection angles. Balanced torque more closely matches SPARC operation, which has no neutral beams [2]. In the comb-line antenna, power is fed from one of the two coax ports as shown in Figure 2 (c), resulting in a single-signed $P(n_{||})$ peak. The solution to producing a symmetric $P(n_{||})$ power spectrum is to feed the antenna with a coax at the center strap, and remove power at both ends for a total of three coaxial cables as opposed to two.

In addition to the limitation of requiring three coaxial feeds in place of two (and associated increase in the complexity of the feed circuit), a further limitation with this feeding scheme is that the selectivity of the $P(n_{||})$ spectrum is not as high as previous designs for end-fed TWA [22] antennas due to the two halves of the center-fed TWA behaving as two smaller, oppositely directed comb-line end-fed TWA antennas. The green arrows in Figure 2 (c) and (d) illustrate this idea: in (c) the antenna is one end-fed 11-strap comb-line, while the 11-strap center-fed antenna in (d) is effectively two oppositely directed 6-strap end-fed comb-line antennas, back-to-back. Fewer straps lead to less selective peaks, and some undesirable overlap of the peaks also occurs when two are oppositely directed. These shortcomings are made up by the fact that for this application and for ICRF heating in general, $n_{||}$ selectivity is less important than for current drive applications – being away from low $n_{||}$ coaxial mode excitation and below the point where electron heating becomes dominant for the high harmonic fast wave regime is acceptable here.

It has been shown that impurity production from ICRF antennas is reduced when image currents are canceled on the antenna box [30], which can be achieved by controlling the phase and power ratio on the last two straps on either side of the antenna, with a phase difference of π and higher power on the inner strap being effective. To this end, two additional passive straps are added after the coax ports which remove power from both ends of the antenna. The design goal was to use the capacitors on these straps to yield the desired power ratio and phase difference. This new configuration is shown in Figure 2 (b), and the RF traveling wave power direction is shown in Figure 2 (d). Although passive end straps could be used with an end-fed TWA, the design is simplified in the center-

fed TWA in that the symmetry lets both the left and right passive strap capacitor values be the same. This new pair of straps comes with the drawback of lengthening the antenna, and could adversely affect the power spectrum.

Key geometric quantities are shown in b) with blue dashed lines and are quantified later. A balance must be met between the design goals of impurity-minimizing power ratio and phase difference, the antenna structure reflection coefficient S_{11}, and power spectrum control including peaks at the desired $n_{||}$, and low power near $n_{||} = 0$ to avoid coaxial mode excitation.

1.4 High Field Side Launch

In order to engineer a robust actuator for producing a fast deuterium population that meets the physics requirements discussed, the combined engineering solution of using a TWA in conjunction with high-field side (HFS) launch was pursued. This combination is extremely attractive as both a fast particle source, as well as for testing the TWA HFS launch as a robust integrated solution for later applications of ICRH heating in reactor-class devices.

The HFS offers numerous advantages for ICRH from both a physics and an engineering point of view. Exhausted power is found experimentally to be expelled towards the scrape-off layer on the low-field side (LFS), putting a LFS ICRH antenna directly in the path of this high particle and heat load [31]. To combat this, the antenna is necessarily moved farther from the last closed flux surface (LCFS), which for ICRH decreases coupling. As the antenna moves further from the plasma, smaller $n_{||}$ are required to maintain a given coupling, as the evanescent region (the region between the antenna and the R-cutoff [3]) is more reflective for smaller wavelengths. However, very low $n_{||}$ can excite undesirable "coaxial modes" [22], where the conductive device wall and the conductive plasma surface act effectively as a coaxial cavity for device-sized modes. On the HFS, the antenna can both be placed closer to the LCFS due to lower heat and particle loads, and take advantage of the HFS scrape-off layer itself being smaller, improving coupling [32]. In addition, the HFS has nearly zero fluctuation-induced fluxes when double-null equilibria are used [32], which provides a more consistent plasma impedance seen by the antenna than on the LFS. The angle of incidence between the toroidal and field directions is also reduced on the HFS, allowing for easier implementation of field-aligned antennas for longer TWAs. Avoiding the LFS's high heat loads, damaging particle exhaust, and highly turbulent regions improves the survivability of antenna components and is highly desirable when moving toward a steady-state reactor.

Most of the challenges with HFS launch stem from the geometric constraints, including a smaller surface area and more difficult transmission line routing. On DIII-D, routing the transmission lines under the device tiles will be required, should this system be installed there; however, scoping such routing is left to future work. In future higher field machines, a further limitation of the HFS is the larger amount of structural support required to handle the larger magnetic forces present on the HFS, all while in the more tightly geometrically constrained space.

2 Physics Scoping with GENRAY/CQL3D

Scoping of beam power, RF power, and $n_{||}$ were performed in GENRAY and CQL3D with the zero-orbit-width approximation. The main goal of this section is to inform the initial design features of a proof-of-concept flat center-fed TWA that meets the physics mission of channeling power to the beam ions while maintaining good SPA from the HFS of the machine.

A target shot was identified on DIII-D due to its good SPA at relatively low RF powers. This shot is high $q_{\min}$ discharge 147634, which has a toroidal field of 1.66 T, with 6 keV ions and 4.5 keV central electrons. General trade-offs in selecting this shot came from the following considerations: 1. hotter plasmas have lower collisional drag, so maintaining a popula-

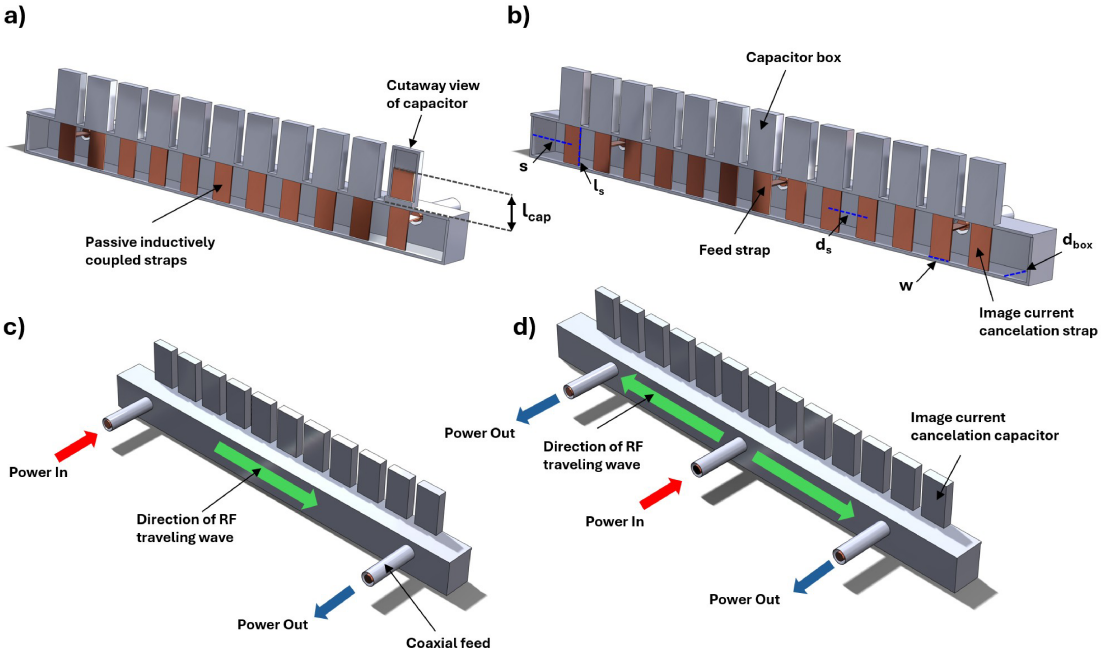

Figure 2: Comparison of an end-fed TWA (a) and a center-fed TWA (b), the latter being the subject of this paper. The end-fed TWA antenna traveling wave moves as shown by the green arrow in c), where one coax inputs power and the second removes it. The center-fed TWA in d) shows that power is fed by the center coax, and is removed by both end coax cables. Also shown on the figure are key geometric quantities discussed in later sections.

tion of fast ions is easier for the same input power, 2. lower field and higher density both increase $V_{\rm fast}/V_{\rm A}$ for a particle with fixed thermal velocity $V_{\rm fast}$. An advantage of high $q_{\rm min}$ discharge 147634 over several of the other shots considered was its relatively lower central field and higher density of $6{\times}10^{19}$ m^{-3}.

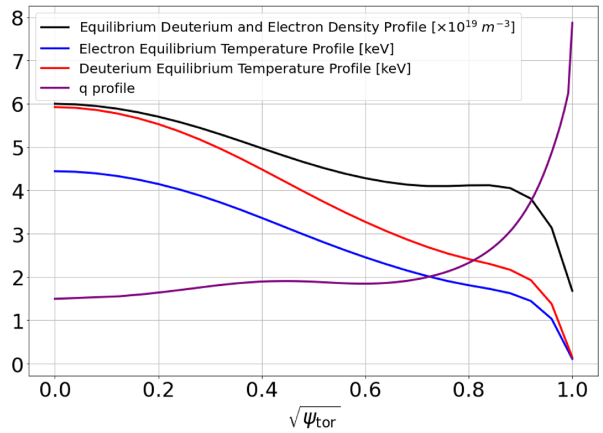

Figure 3: Density, temperature, and q profiles for DIII-D high $q_{\rm min}$ discharge 147634 are shown.

High $q_{\rm min}$ discharge 147634's density, ion temperature, electron temperature, and safety factor q profiles are shown versus the square root of the normalized toroidal flux in Figure 3. The higher thermal ion temperature relative to the electron temperature was found previously to lead to higher bulk ion heating [13], which for this application is deleterious because the goal is to channel power to the fast NBI ions, not to the bulk ions.

The choice of the 96 MHz frequency, positioning the 8th harmonic on high $q_{\rm min}$ discharge 147634 near the center of the discharge, stemmed from several considerations. In the pass band of a TWA antenna, the center of the band for identical strap capacitances will see a mean strap phase difference $\Delta\phi$ of $\pi/2$ if a simple lumped element LRC circuit model is used to model the mutually coupled straps [33]. The assumption of identical strap capacitance is not the case in the final design produced here, but was used as a starting point to get a sense for the overall array geometric dependen-

cies on the choice of frequency (it will be shown later that $\Delta\phi = \pi/2$ is a fairly good estimate of the average phase difference in the final design). Assuming for now the $\pi/2$ inter-strap phasing, a full parallel wavelength is $\lambda_{||} = 4d_s$, where d_s is the distance between strap centers. At a frequency $f = \omega/2\pi$, the desired $n_{||} = k_{||}c/\omega = c/f\lambda_{||}$ is 5, as will be explained shortly, resulting in a harmonic dependent strap spacing given by $d_s = \frac{c}{4n_{||}mf_0}$, where m is the harmonic number and f_0 is the deuterium cyclotron frequency $f_0 = \Omega_d/2\pi$ at the desired location, here slightly on the low-field side of the mid-plane ($B \approx 1.57$ T) so the m-1 harmonic also could contribute to ion damping. For good selectivity in the $n_{||}$ spectrum, at least 13 straps (including the image current cancellation straps) were desired (6 in each direction for the center-fed TWA, double-counting the center feed strap), and this was to fit in less than 1/3 of DIII-D's central stack circumference. To achieve this, the lowest harmonic number m can be solved for which $12d_s < \frac{1}{3}2\pi R_s$, where R_s is the central stack radius of 1 meter. Plugging in these values for Ω_d, $n_{||} = 5$, yields an $m = 8$ harmonic d_s of 15.625 cm, extending 29% around the central stack for 13 straps, and an $m = 7$ d_s of 17.857 cm, extending 34% around the central stack.

To meet the constraint of 13 straps extending less than one-third around the central stack, $m = 8$ was selected, leaving some room for the antenna box edges, and selected if neutral beam absorption remained strong enough at this harmonic, as will be shown to be the case. This also had the advantage of allowing for shots with higher B with no change of antenna frequency: higher central B would result in lower harmonics, which provide stronger damping, but also risk bulk deuterium heating if harmonics are low enough. Choosing $m = 8$ for this relatively lower field case gives margin for higher field shot harmonics to remain large enough to avoid bulk heating. For these reasons, 96 MHz was selected as the design frequency.

GENRAY was run on an EQDSK equilibrium file with the cold plasma fast wave dispersion root selected and Imag($n_\perp$) set to the fast wave option to model fast wave damping. The grill settings give an $n_{||}$ spread of $\pm$ 0.2 about the peak. Three species were modeled in GENRAY: thermal bulk deuterium ions and electrons with profiles given in Figure 3, and a lower density hotter "fast" deuterium ion species to mimic the neutral beam population. A density profile scaling of 0.1 and a temperature profile scaling of 8 relative to the ion density and temperature profiles in Figure 3 were used. This was needed in GENRAY to provide a more realistic initial guess for ray damping to fill out the tail of the distribution function (GENRAY assumes linear damping on a Maxwellian distribution of particles for a given species) before it was fed to CQL3D for full self-consistent damping with CQL3D's NBI Freya package. GENRAY was run once per case, and the rays output by GENRAY were then input to CQL3D. A self-consistent electron and deuteron ion species were used in CQL3D so direct investigation of power coupling to each species was possible, including collisional power partitioning of fast ions slowing on ions and electrons (this is the "general species" option in CQL3D). CQL3D was iterated until steady state. All deuterium cyclotron harmonics in the discharge for 96 MHz were included, as well as direct electron damping.

Broad scans of beam power and RF power were performed at $n_{||} = 5$ to investigate where good SPA was achieved. Beam power was varied between 0, 2.5, 5, 7.5, and 10 MW in CQL3D to reflect available DIII-D beam power, with 80 keV beam deuterons assumed. For simplicity, only one injected neutral beam angle was used along with a single signed $n_{||}$ during this scoping. This is partially justified by assuming symmetry to a case where the opposite signed $n_{||}$ and neutral beam toroidal launch direction are used. However, it is important to note that if balanced torque is desired, it is only possible for 5 MW of neutral beam power due to only one of the four 5 MW beam being positionable in the opposite toroidal direction on DIII-D [29]. The general desired goals here were to achieve good SPA with 5 MW of NBI and $\leq$ 1 MW of RF power.

The influence of beam power on SPA can be seen in Figure 4, which plots the equilibrium (black), deu-

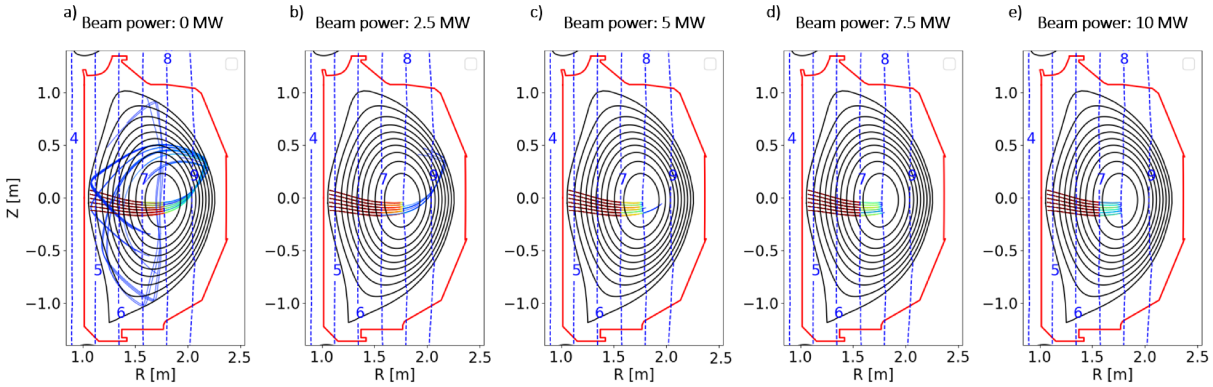

Figure 4: Ray power absorption for different neutral beam powers. Color in ray indicates power remaining in ray relative to launched power. Blue dashed vertical lines are deuterium harmonics and are labeled with the harmonic number. Ion absorption mainly occurs in discrete steps at the 7th and 8th harmonics.

terium cyclotron harmonics (blue dashed), and GENRAY rays. The rays are colored by the power remaining in the ray relative to launched, and are plotted until 85% of the ray power has been absorbed. Steep color gradients in a ray indicate where power is absorbed by the plasma. The ray damps gradually due to electron damping, and at discrete locations on the deuterium cyclotron harmonics. In this application, good SPA and high ion channeling are complementary: high ion heating indicates large cyclotron damping on the first pass. 5 MW of beam power is selected for its high SPA and is used for further scans of $n_{||}$ and of RF power.

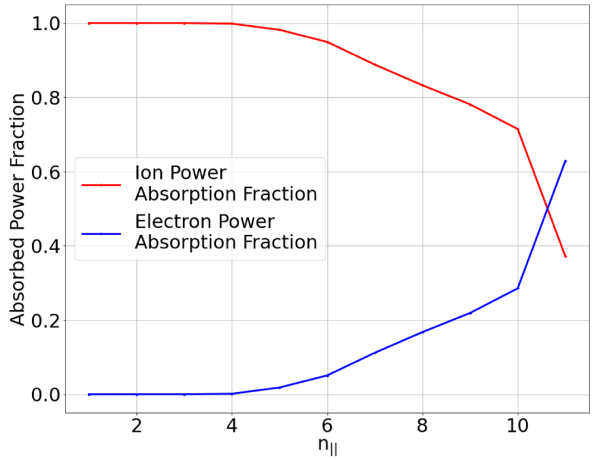

Figure 5: The power absorption partitioned to the ions and to the electrons is dependent on the launched $n_{||}$, with higher $n_{||}$ leading to preferential electron absorption.

Next, the ratio of power channeled to ions versus to the electrons during the first pass of the rays in response to different peak $n_{||}$ was investigated. To accomplish this, $n_{||}$ was varied in steps of 1 from 1 to 11. Figure 5 shows that as $n_{||}$ is increased, there is a larger fractional power absorbed by the electrons for these shorter parallel wavelength waves. This trend matches the results predicted in [9] and modeled in [13].

Given this result, lower $n_{||}$ are clearly desirable. However, having too low of an $n_{||}$ is unacceptable as global coaxial modes can be excited [22]. Coaxial modes are important when a peak lies near $k_{\text{peak}} = k_0$ (see discussion around Figures 7 and 8 in [22]), where $k_0 = 2\pi f/c$ is the free-space wave number. This corresponds to peaks near $n_{||} = 1$. Determining if the selected $n_{||}$ is far enough from 1 to avoid coaxial mode excitation can be done after optimization is complete: if spectrum peaks are excited near $n_{||} = 1$ for increased plasma loading (decreased evanescent layer), then those peaks are too large at those low $n_{||}$ values and should be reduced. Given these considerations, an $n_{||}$ near 5 is selected as the design goal of the antenna, as this is the largest $n_{||}$ before the gradual increase in electron absorption begins. Note that the fractional power absorption to thermal ions is sensitive to T_i/T_e [13], so strictly this scan should be redone if other shots with different values for this ratio are present. However, this is not the dominant effect when enough fast

ion damping is present, as is the case here [13].

For 5 MW of NBI and $n_{||} = 5$, an RF power of 700 kW was found through further GENRAY/CQL3D scoping, this time varying the RF power between 500 and 1,000 kW in steps of 100 kW. The RF power level weakly changed the SPA: electron first-pass absorption was largely independent of RF power as electron damping occurred smoothly along many passes of the rays, while ion first-pass absorption increased with RF power linearly with the launched power, leading to weakly increasing ion selectivity in the first pass for larger RF powers. SPA was nearly constant due to SPA already being near one at the lowest RF power looked at (500 kW). Future considerations of $\beta_{\mathrm{EP}}/\beta_{\mathrm{th}}$ will determine the appropriate RF power level.

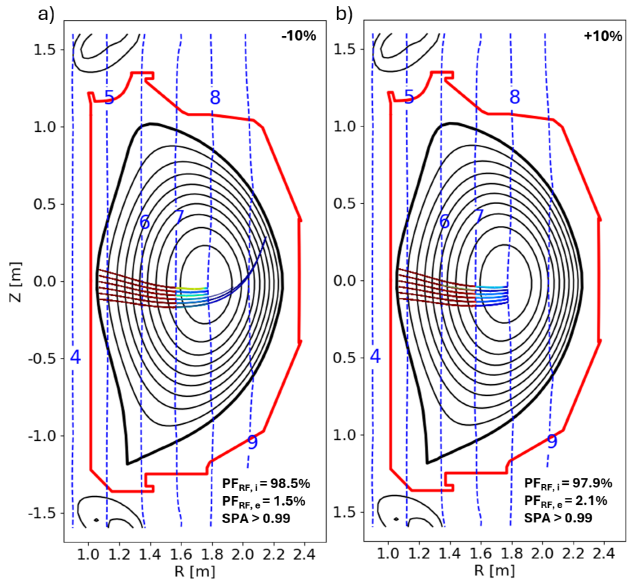

Figure 6: Rays plotted to 99% power deposition, and RF power fraction ($\mathrm{PF_{RF}}$) to ions and electrons for $\pm 10\%$ variation in density and temperature profiles for 5 MW beam, 700 kW, $n_{||} = 5$ case. Performance is acceptable in both the a) -10%, and b) +10% cases.

For the 5 MW beam, 700 kW, $n_{||} = 5$ case, the effect of varying the equilibrium density and temperature profiles on ion RF selectivity and SPA was investigated. The density and temperature profiles were varied by $\pm 10\%$, with the resulting performance changes shown in Figure 6. In Figure 6 a), the profiles in Figure 3 were decreased by 10%, and in b) were increased by 10%. Rays in Figure 6 are plotted until 99% of the initial power is left, indicating both achieve good (> 0.99) SPA. Figure 6 b) has slightly higher electron damping, with 2.1% of the launched RF power going to electrons relative to 1.5% in a). This difference is due to the increased electron temperature and the slightly shallower neutral beam deposition than seen in a) for the lower density case. Overall, the ion heating performance and SPA are largely insensitive to $\pm 10\%$ changes in density and temperature, indicating the scheme is robust to core profile fluctuations. This is not surprising: the main mechanism providing good ion channeling and SPA is the interaction between the RF waves and the neutral beam fast ions, not the bulk profiles, so long as the density profile does not block too much of the beam's penetration.

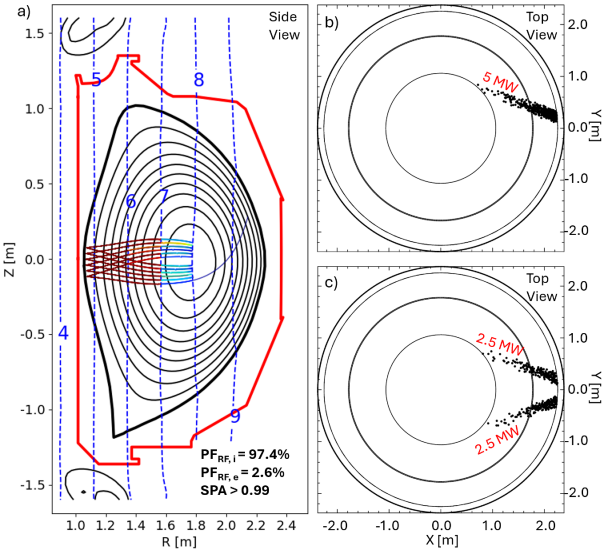

Figure 7: a) Symmetric $n_{||} = \pm 5$ rays shown until 99% ray power deposition, 350 kW per sign. b) and c): beam deposition, top view of machine. 400 points selected from the 30,000 NBI particles per time step to represent the NBI fast ion birth points. b) single-signed 5 MW beam used during scoping, c) two 2.5 MW beams used for co/counter symmetric case.

A GENRAY/CQL3D run was performed on the 5 MW beam, 700 kW, $n_{||} = 5$ case with both $n_{||}$ signs and co/counter beam directions. The 700 kW of RF power was divided into the two $n_{||}$ lobes, each get-

ting 350 kW. The beam power was divided into the two neutral beam directions, each receiving 2.5 MW. In Figure 7 a), the rays are shown until 99% ray power deposition, displaying the performative SPA seen during scoping. In b) and c), a top view of the machine is shown, with 400 of the 30,000 per iteration NBI fast ion birth points indicated by black dots, which are representative of the beam deposition. In Figure 7 b), the single-angled beam used during scoping is shown. In c), the co/counter configuration used in the case that produced the rays in Figure 7 a) is shown, with the 5 MW of beam power split evenly between the two beam angles.

The distribution function of the deuterium ions for the co/counter beam, symmetric $n_{||}$ case was pitch-angle integrated and is plotted at $\sqrt{\psi_{\text{tor}}} = 0.01$ (near the 8th cyclotron harmonic) in Figure 8, with a) depicting the pitch-angle integrated density on a linear scale, and b) on a $\log_{10}$ scale. In red dashed is high q_{min} discharge 147634's Maxwellian distribution for the 6 keV bulk deuterium temperature, and in blue is the CQL3D distribution function containing the bulk, neutral beam, and RF effects. The sharp corner at 80 keV is due to the NBI, and the broader high-energy tail is due to the RF heating. Plotted above is a $V_{\text{fast}}/V_{\text{A}}$ axis and a $\rho_{\text{L,EP}}/a$ axis, using the field strength and density at $\sqrt{\psi_{\text{tor}}} = 0.01$ to calculate V_a and $\rho_{\text{L,EP}}$. Recall that in Figure 1, SPARC has a $V_{\text{fast}}/V_{\text{A}}$ roughly of 1.55, and ITER alpha of 1.7. The values of $V_{\text{fast}}/V_{\text{A}}$ and $\rho_{\text{L,EP}}/a$ for SPARC and ITER alpha are plotted along the $V_{\text{fast}}/V_{\text{A}}$ and $\rho_{\text{L,EP}}/a$ axis in a) in green and orange, respectively. Figure 8 a) clearly displays elevated ion density at these $V_{\text{fast}}/V_{\text{A}}$ ratios, however quantifying if the achieved β_{fast} is high enough will be reserved for future work which will include an Alfven eigenmode (AE) solver using distribution functions as input. The log plot in Figure 8 b) demonstrates that the RF tail extends to nearly 3.5 MeV before Maxwellian falloff returns, however, densities at these energies are low.

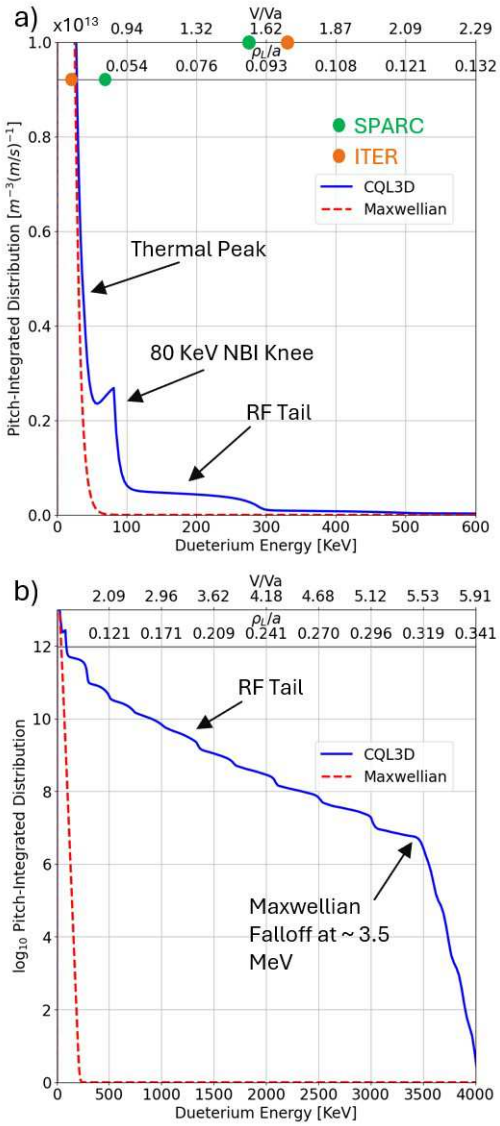

Figure 8: The pitch-integrated distribution function for $\sqrt{\psi_{\text{tor}}} = 0.01$ on a) a linear density scale and b) on a logarithmic density scale. Plotted on top of each sub-figure is the $V_{\text{fast}}/V_{\text{A}}$ and $\rho_{\text{L,EP}}/a$ ratio, with the SPARC and ITER alpha values for these from Figure 1 plotted with green and orange dots, respectively.

The $\rho_{\text{L,EP}}/a$ value of the ions with $V_{\text{fast}}/V_{\text{A}} = 1.55$ (the SPARC value) can be estimated for this discharge at $\sqrt{\psi_{\text{tor}}} = 0.01$. The distance between the equilibrium center and the HFS LCFS is 0.72 m, so treating this as a, the Larmor radius normalized to a at $\sqrt{\psi_{\text{tor}}} = 0.01$ for deuterium is $m_{\text{D}} V_{\text{fast}}/a q_{\text{D}} B_{\text{center}} = 0.089$, which is larger than SPARC's 0.045 value or ITER's roughly

0.025 value. Assuming for now the energy distribution shown in Figure 8 remains fixed on the absolute energy scale, the $V_{\rm fast}/V_{\rm A}$ and $\rho_{\rm L,EP}/a$ axes can be shift by changing B and density. Raising B will shift both axes rightward at the same rate due to both depending on inverse B. Density will independently shift $V_{\rm fast}/V_{\rm A}$ proportional to the square root of density. So, a strategy to match SPARC or ITER parameters better could be to raise B, which would shift both axes rightward until $\rho_{\rm L,EP}/a$ is positioned at an acceptable value of pitch-integrated particle density (this pitch-integrated density should correspond to an acceptable $\beta_{\rm EP}/\beta_{\rm th}$), followed by increasing density so $V_{\rm fast}/V_{\rm A}$ can be reduced until the desired device value for this parameter is co-located with $\rho_{\rm L,EP}/a$. Raising density will affect SPA, ion absorption, and beam absorption, and is limited by β and Greenwald limits [34].

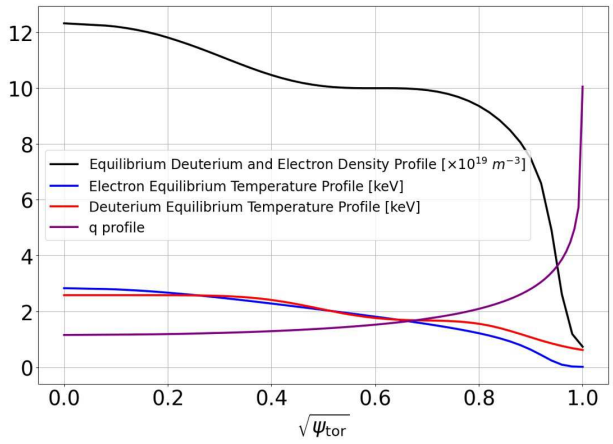

Figure 9: Density, temperature, and q profiles for DIII-D Super H-mode discharge 201991.

For example, to fully cause the two green SPARC points in Figure 8 a) to overlap, the on-axis field and density would need to be increased to 2.4 T and 2.37×10^{20} m^{-3}, which is above DIII-D's maximum limits. Increasing B and n to near DIII-D's limits was investigated in "Super H-mode", which provided access to high density and high field. Super H-mode shot 201991 was used, with an on-axis field of 2.1 T and on-axis density of 1.23×10^{20} m^{-3}. This shot's density, temperature, and q profiles are shown in Figure 9. For no change in the antenna frequency and $n_{||}$, the higher field resulted in lower harmonics (6th harmonic near central axis), and a much poorer neutral beam penetration depth due to the larger density. Harmonics are further spaced apart, with two instead of three main harmonics contributing to fast ion absorption, reducing performance, as pointed out in [13]. A lower seed population of beam ions lowered SPA and ion resonant heating. To compensate for this effect, the neutral beam power was first raised to 5 MW in both the co and counter directions, for 10 MW total (this is the upper limit for symmetric co/counter beams). This case is shown in Figure 10 a), with rays plotted over their first pass across the plasma. Notably, SPA was reduced to 72%, and the ion first-pass power fraction $\mathrm{PF}_{RF,i}$ to 75.1%. As will be shown shortly, the produced distribution function for this case saw an enhanced high-energy tail over high $q_{\rm min}$ discharge 147634, so even though the RF performance has been reduced, this no-redesign case with co/counter beams may still be acceptable.

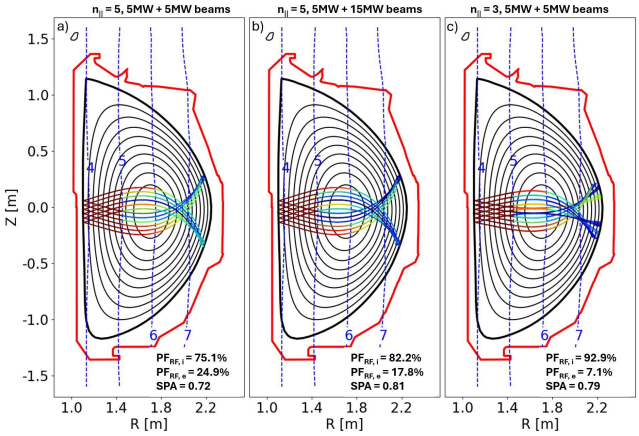

Figure 10: Rays plotted for first pass across plasma for Super H-mode shot 201991. a) $n_{||} = \pm5$, 5 MW beams in both directions (10 MW total). b) $n_{||} = \pm5$, 5 MW beam in reverse direction, 15 MW beam in forward toroidal direction (20 MW total). c) $n_{||} = \pm3$, 5 MW beams in both directions (10 MW total). Power fraction PF to ions and electrons, and SPA, are indicated.

For no change in the antenna design, but relaxing the constraint of balanced co/counter beams, the SPA and

$PF_{RF,i}$ were improved by increasing the co-directed beam power to 15 MW, leaving the counter-directed beam power at its 5 MW maximum for 20 MW total. This resulted in an SPA of 81%, and an $PF_{RF,i}$ of 82.2%, shown in Figure 10 b). Finally, in Figure 10 c), the beam powers were both set at 5 MW, but allowance was made for a changed antenna $n_{||}$ from ± 5 to ± 3. The SPA was improved to a lesser extent than the 20 MW beam case to 79%, but the ion power fraction was increased to 92.9%. This $n_{||} = \pm 3$ option may not leave enough margin in the $n_{||}$ spectrum from undesirable coaxial modes, and would require a different antenna optimization from the cases in Figure 10 a) and b) and Figure 7 a).

The resulting pitch-integrated distribution functions for the three Super H-mode options just discussed are shown in Figure 11, with a linear scale shown in a) and a $\log_{10}$ scale in b). In red dashed is the Maxwellian distribution for the 2.58 keV bulk deuterium temperature. The three cases investigated in CQL3D: 5 MW co/counter beams, 5 MW co, 15 MW counter, and $n_{||}$ = ± 3 are shown in blue, salmon, and purple, respectively.

There are several notable differences between Figure 11 and Figure 8. First, by construction, the green SPARC points and orange ITER points on the $V_{\text{fast}}/V_{\text{A}}$ and $\rho_{\text{L,EP}}/a$ axes are closer together and entirely over the non-Maxwellian portion of the distribution function, with the SPARC points entirely in the RF tail region. This improved matching came at the cost of reduced neutral beam performance: the neutral beam knee density has been reduced even at these much larger neutral beam powers due to the increased bulk plasma density. The RF tail in a) does not feature a visible increase in the 100 keV - 300 keV range when compared to Figure 8 a), but sees a much stronger high-energy tail in Figure 11 b) out to past 4 MeV, nearly 1000 times larger at 3.5 MeV than in Figure 8 b) for the two $n_{||} = \pm 5$ cases, and even higher for the $n_{||} = \pm 3$ case. All three of these options produce improved high-energy tails over Figure 8, the simplest option (no change to antenna, co/counter beams set to 5 MW each) may be acceptable so long as the 72% SPA does not lead to too many deleterious effects for the 700 kW launch power.

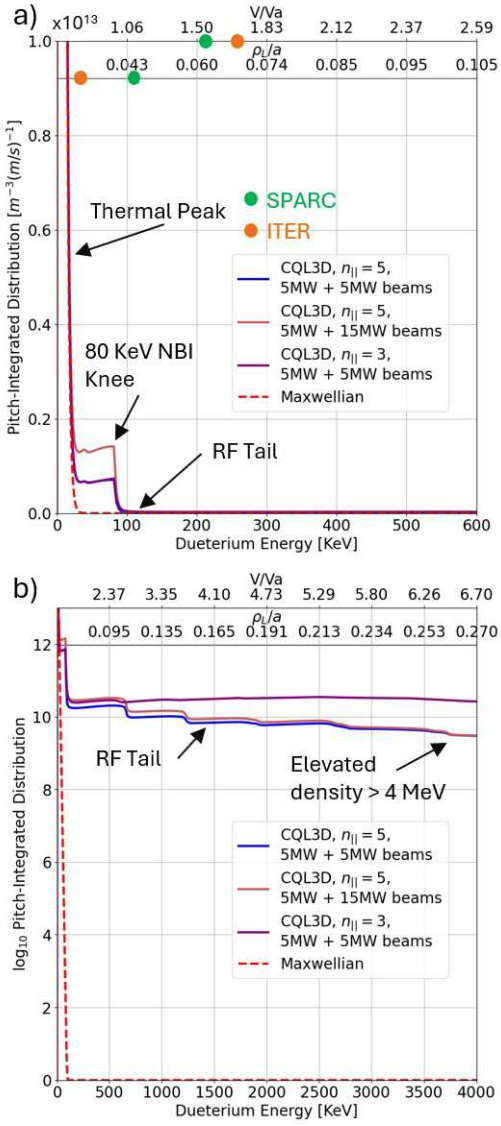

Figure 11: Super H-mode shot 201991 pitch-integrated distribution function for $\sqrt{\psi_{\text{tor}}} = 0.046$ on a) a linear density scale and b) on a logarithmic density scale. Plotted on top of each sub-figure is the $V_{\text{fast}}/V_{\text{A}}$ and $\rho_{\text{L,EP}}/a$ ratio, with the SPARC and ITER alpha values for these from Figure 1 plotted with green and orange dots, respectively. The three CQL3D options for this shot are shown in blue, salmon, and purple, indicated in the legend.

Given that the distribution functions here were cre-

ated using CQL3D in the zero-orbit approximation mainly for scoping candidate shots for SPA and good ion absorption, the distributions shown in Figures 8 and 11 should be taken as a starting place; the limitations will be discussed in the Discussion and Limitations section. The main takeaway here is that the RF tail does contain elevated density at SPARC and ITER-relevant values for $V_{\mathrm{fast}}/V_{\mathrm{A}}$. Separately, there is also elevated particle density at energies corresponding to SPARC and ITER $\rho_{\mathrm{L,EP}}/a$, but these lie within the NBI and bulk parts of the distribution for high q_{min} discharge 147634 unless the on-axis field and density are raised to the level of Super H-mode shot 201991, with future work required to retire modeling limitations. For the same antenna parameters of $n_{||} = \pm 5$ and 700 kW of RF power, high q_{min} discharge 147634 achieved better SPA and RF performance at lower beam power, while Super H-mode shot 201991 achieved better matching to target devices in the non-Maxwellian portion of the distribution function and a larger tail at very high (>1 MeV) energies at the cost of reduced SPA.

3 RF Network Optimization Method

The method used to design the TWA antenna here builds on work by Ragona [20], where the antenna body and capacitors are separately analyzed in an electromagnetic finite element analysis (FEA) solver to extract the component S matrices and port characteristic impedances for use in a Python RF circuit modeling package. The antenna body is a 16 port component (three coaxial cables, two image current cancellation capacitors, and eleven main strap capacitors). The capacitor is a 1-port device. COMSOL [35] was used as the finite element tool for the optimization stage, with two separate COMSOL models created for the antenna body and the capacitor. In the antenna body model, the full 16×16 S matrix was computed by scanning ports, for frequencies between 81 and 111 MHz in steps of 1 MHz. The 1×1 capacitor S matrix was scanned over the same frequency range and for capacitor lengths l_{cap} between 5 and 19.4 cm in steps of 0.2 cm (this length range was initially smaller, and expanded during optimization when a length value was set to the maximum of the range). Interpolation was used in the optimizer for the 1×1 capacitor S matrix as a function of length, so the lengths took on continuous values during the optimization.

Next, the Python package scikit-rf [36] was used to read in the COMSOL S matrices and create functions that interpolate the real and imaginary parts of S over the frequencies and lengths scanned in COMSOL. Python objects representing the antenna body and capacitors were wired together in circuits for rapid scans of capacitor lengths. The circuit model can be probed for the circuit reflection coefficient, and the current magnitude and phase into the capacitors. This circuit model then can be quickly scanned for optimized whole antenna properties. A schematic of this method is shown in Figure 12, with the wiring between the antenna body object to the capacitors shown in (a). In b), the full COMSOL model represented in a) is shown, which is used after the optimization is finished to confirm that the full wave solver predicts the same device properties as the Python circuit model. In (c) and (d) the individual COMSOL models used to create the components in (a) are shown, with port de-embedding used in both to ensure the S parameters were extracted at the same point in both models for circuit construction.

A challenge with this method is that although the Python circuit model does give access to the complex currents into each of the capacitors in Figure 12 a), it gives no spatial distribution because the network model is 0D. However, the power spectrum P($n_{||}$) was desired to be part of the Python circuit model optimization. To achieve this, the straps were treated as a series of rectangular current pulses of width matching the strap width w and inter-strap separation distance $\delta = d_s$ - w, with magnitudes $|I_j|$ and phases ϕ_j given by the corresponding complex current predicted by the Python model for the jth capacitor connection. An an-

alytic expression for the Fourier transform of a series of arbitrary-phased complex rectangular pulses is given by Equation 1.38 in [37], repeated here in Equation 2:

$$P(n_{||}) \propto \frac{\sin^2(n_{||}\frac{w\omega}{2c})}{n_{||}^2} \sum_{j=0}^{N-1} |I_j| e^{-i(\beta_j+\phi_j)} \sum_{j=0}^{N-1} |I_j| e^{i(\beta_j+\phi_j)},$$
$$\beta_j = n_{||}\frac{\omega}{c} j(w+\delta). \tag{2}$$

Here, ω is the angular frequency, N is the number of straps, and c is the speed of light. This method allowed for very efficient calculation of the power spectrum properties during the Python optimization. Limitations in using this analytic expression to calculate $P(n_{||})$ are that the rectangular pulse model ignores any variation in current along the strap face, the strap's finite vertical extent, and any currents driven on the antenna box face not on the straps. All power spectra shown in subsequent figures in this paper are from the full FEA model, and are not from this circuit model analytic expression.

To optimize the TWA antenna design, a cost function in Python is defined that is positive definite and increases in value as any particular design goal becomes further from its design target. The cost function is given by

$$\begin{aligned}\text{COST} = \alpha_0 \sum_f (S_{11,\text{db}}(f) - S_{11,\text{db,target}})^2 \\ + \alpha_1 \frac{(n_{||,\text{peak}} - n_{||,\text{peak,target}})^2}{n_{||,\text{peak,target}}^2} + \alpha_2 \frac{P(n_{||}=0)}{P_{\max}} \\ + \alpha_3 \frac{\sum_p P(n_{||_p})}{N_p P_{\max}} + \alpha_4 \frac{(\Delta\phi - \pi)^2}{\pi^2} + \alpha_5 \frac{(\text{PR} - \text{PR}_{\text{target}})^2}{\text{PR}_{\text{target}}{}^2}.\end{aligned} \tag{3}$$

In the cost function, the sum in the first term runs over discrete frequency points over which the reflection coefficient is desired to be minimum, here 92 to 100 MHz was used, with points separated by 1 MHz. Note that although the cost function minimization took place within this frequency window, later figures show the optimized antenna's frequency response over a wider frequency range. The target reflection coefficient used $S_{11,\text{db,target}}$ is -35 dB, with the design goal of being below -20 dB around 96 MHz within roughly a ±1 MHz window. The weight α_0 for this term is equal to 1, and the other α_i terms weight the other terms of the cost function against this first term. The second term in Equation 3 controls how far the power spectrum peak is from the desired value $n_{||,\text{peak,target}}$. The third term is included to reduce the low $n_{||}$ coaxial mode by adding a cost related to the power spectrum value at $n_{||} = 0$. The fourth term allows for selecting N_p manual points p where the power spectrum should also be minimized, this was implemented to remove peaks at low $n_{||}$ that were slightly away from $n_{||} = 0$. The fifth and sixth terms both reduce image currents on the antenna box by controlling the power ratio PR and the phase difference $\Delta\phi$ between the image current cancellation straps and the outer traveling wave straps. The PR is defined as I_n^2/I_p^2, where I_n is the current magnitude in the final traveling wave strap, and I_p is the current magnitude in the image current cancellation strap. Here, the target power ratio $\text{PR}_{\text{target}}$ was 2, and the phase difference target was π. The coefficients α_1 through α_5 are parameters that need to be manually tuned by the antenna designer as trade-offs are made between the TWA's performance in reflection coefficient, power spectrum peaking, coaxial mode excitation, and image current cancellation.

The cost function is minimized by varying C_p and C_1 through C_{11} using SciPy's optimization tools. Due to the complicated non-linear structure of the cost function with respect to varying the capacitances, SciPy's *minimize* algorithm, which was used in past work for a similar optimization only for the reflection coefficient [20] of a comb-line end-fed TWA, was found to be very sensitive to the chosen initial conditions. Instead, SciPy's global optimization tool *differential_evolution* was selected to overcome the initial condition sensitivity. Differential Evolution is a genetic algorithm

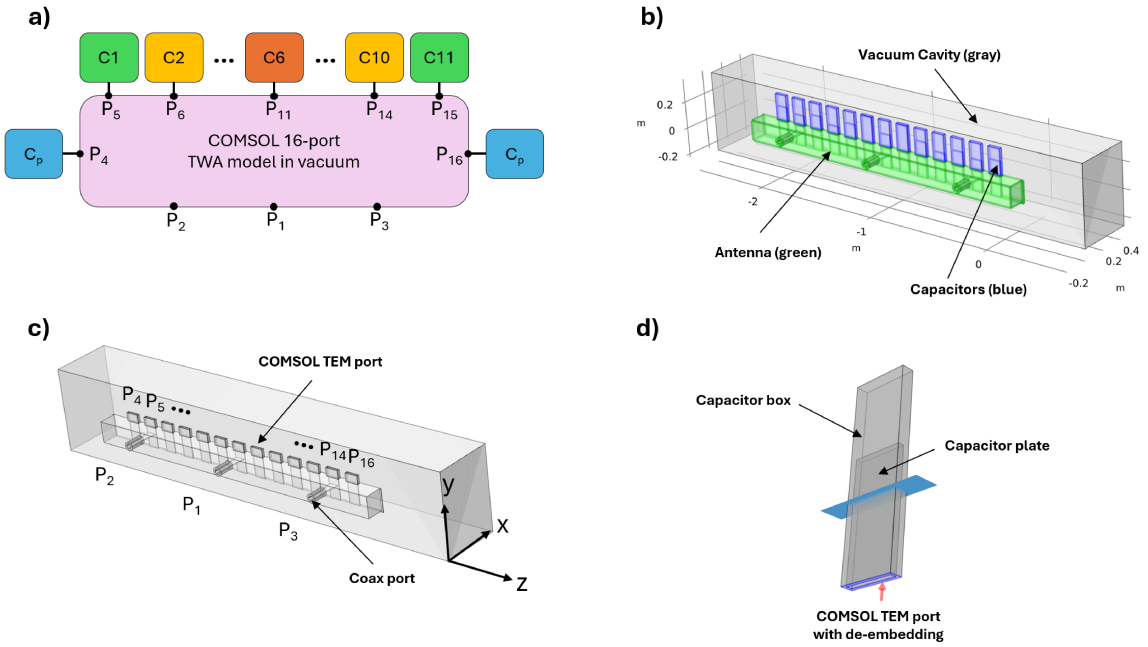

Figure 12: (a) Individual RF networks combined into the larger full antenna network. (b) Transparent view of the COMSOL components represented in (a). A TEM boundary condition was used for the rectangular ports at the cut point of the capacitors. c) The antenna 16 port model, which is scanned over frequency. d) The capacitor model which is scanned over frequency and plate length.

that does not calculate cost function gradients to find minima, and instead creates a population of individual solutions known as agents, which are combined to generate successive populations based on agent performance with respect to the cost function [38]. It is not guaranteed that the global minimum is found, however. The *differential_evolution* algorithm queries the cost function many thousands of times during optimization, demonstrating the need for the simpler Python scikit-rf model: the number of equivalent full FEA runs required to get the same information from COMSOL would be prohibitively expensive, especially in Section 4, when a cold plasma load is used.

Table 1 a) details the α_i parameters used in the final optimization. The strategy for settling on these values was as follows: first, α_1 through α_5 were set to zero, and the solution was checked to confirm $\alpha_0 = 1$ produced a satisfactory S_{11} band-pass in the desired frequency range. Next, α_1 was turned on, and was manually changed by orders of magnitude, starting at 1, until the Differential Evolution solution's power spectrum $P(n_{||})$ peaks first started shifting to the desired $n_{||,\mathrm{peak,target}}$, followed by slower increases in α_1 to not needlessly weight α_1 too large. Next, α_2 was turned on. The same strategy of increasing the parameter by orders of magnitude until the desired performance attribute was met was done for each subsequent α_i. Using Differential Evolution did come with the drawback in that during this manual tuning of α_1 through α_5, there were in some cases discrete changes in the solution for small changes in α_i, corresponding to a jump in parameter space to the new global minima.

a)

α_1	α_2	α_3	α_4	α_5
$8x10^5$	$1x10^4$	$1x10^3$	$4x10^4$	$3x10^4$

b)

	C_p	C1	C2	C3	C4	C5	C6
l_{cap} [cm]	13.25	14.08	11.04	11.11	10.21	12.39	14.83

c)

	s	l_s	d_s	w	d_{box}	g_{box}	g_{cap}	g_s	t_s
Param. [cm]	16	15	15.625	8	12.5	1.25	0.5	0.25	0.5

Table 1: a) Cost function weights and b) capacitor lengths for optimized antenna. Note $\alpha_0 = 1$. The antenna is symmetric with respect to C_6, so C_7 through C_{11} are not shown in this table. c) Geometric quantities from Figure 2. Quantities not indicated in Figure 2: g_{box} – gap from front of strap to face of antenna box, g_{cap} – gap between capacitor and capacitor box, g_s – thickness increase of strap inside cap box versus outside, t_s – thickness of strap (perpendicular to l_s and w).

The optimization resulted in the capacitor lengths shown in Table 1 b), note that due to the antenna being symmetric about the center strap, only 7 lengths are listed for one-half of the symmetric antenna (C_6 through C_{11} are identical to C_6 through C_1). Table 1 c) shows key geometric parameters of the design, shown in Figure 2 b). The inter-strap spacing d_s was chosen based on the discussion of frequency selection in Section 2, with the image current cancellation strap center to box distance s selected so the overall antenna length was roughly one-third the center stack circumference. The strap length l_s was chosen to be less than a quarter of the free-space wavelength (to constitute a "short strap" – where the current along the strap's long dimension is uniformly phased). At 96 MHz, $\lambda/4 = 78$ cm, giving $l_s = 15$ cm over a factor of 5 margin. The strap width w was chosen to be 8 cm, and the distance between the antenna face and the backplate d_{box} was set to 12.5 cm. The other values in Table 1 c) were not indicated in Figure 2. These are: g_{box} – the gap from the front of strap to the face of the antenna box, g_{cap} – the gap between the capacitor and the capacitor box, g_s – the thickness increase of the strap inside the capacitor box versus outside (slightly larger surface areas allow for larger capacitances for the same capacitor length), and t_s – the thickness of the strap (perpendicular to l_s and w). Future scans of any of these geometric parameters could locate even better optima, but were not performed here.

The optimized electric field Fourier transform was completed in COMSOL's Electromagnetic Waves, Frequency Domain [35] full wave physics tool by modeling the E_y field on a surface directly in front of the antenna box opening, and Fourier transforming E_y^2 in the $\hat{z}$ direction, parallel to the B field direction (the long direction of the model). This result is shown in Figure 13, and features main peaks near the desired $n_{||} = \pm 5$, and a low value at $n_{||} = 0$, avoiding undesired coaxial modes [22].

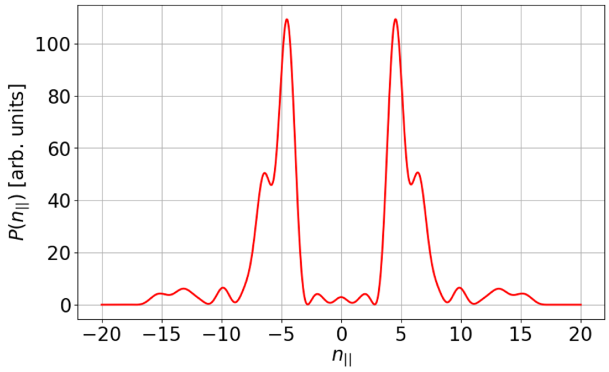

Figure 13: The optimized TWA antenna's vacuum electric field $P(n_{||})$ spectrum given by COMSOL. The spectrum features good selectivity for the design $n_{||} = \pm 5$, while avoiding low $n_{||}$ modes.

Compared to traditional ICRF antennas, which feature fewer straps, the $n_{||}$ selectivity of this center-fed TWA was higher, however, it was not as high as previous designs for end-fed TWA antennas due to the two halves of the center-fed TWA behaving as two oppositely directed smaller end-fed TWA antennas, as previously discussed.

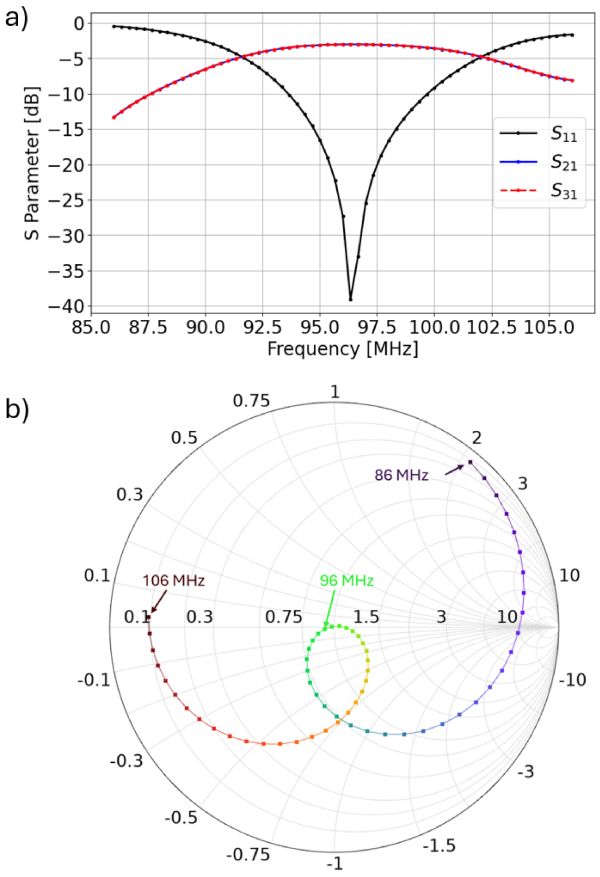

Figure 14: The optimized TWA antenna's vacuum reflection and transmission coefficient response from full COMSOL model. a) frequency scan of S_{11}, S_{21}, S_{31} around the design frequency of 96 MHz. b) S_{11} shown on a Smith Chart, showing the impedance sensitivity on frequency.

The optimized TWA reflection and transmission coefficients from the full COMSOL antenna model (Figure 12, b) are shown versus frequency in Figure 14. Again, a wider range of frequency points than the range used in the optimization is shown to give a broader understanding of the antenna's frequency response. In a), the optimization for S_{11} at 96 MHz is visible in the black curve with a value of -27.3 dB at 96 MHz, and a value of below -35 dB at 96.3 MHz, with a wide window from 95 to 97.5 MHz where S_{11} is below -20 dB. Overlapping in blue and red dashed, the transmission coefficients S_{21} and S_{31} exactly mirror each other, as expected for this symmetric system. In Figure 14 b), the reflection coefficient is shown on a Smith Chart, displaying the resonance near the center of the figure. Color here is used to show frequency, with 86 MHz in purple and 106 MHz in red. The optimization tool successfully met the design condition for S_{11} < -20 dB at 96 MHz. TWA band-pass behavior (rather than a resonant peak) was observed when the cost function weight α_0 was large relative to the other weights. However, the $P(n_{||})$ spectrum was unsatisfactory for the band-pass cases. As the spectrum controlling weights α_1 through α_5 were increased, the band-pass narrowed to a peak. The designer thus has control over the trade-off between the desirability of band-pass behavior, and spectrum and image current control.

As an example, an antenna with a larger α_0 (set to $8{\times}10^4$) and smaller $\alpha_i = 100$, $i \neq 0$, is shown in Figures 15 and 16. In Figure 15, the resulting power spectrum does not avoid potential low $n_{||}$ coaxial modes and has much poorer peak selectivity near the desired $n_{||} = \pm 5$. The achieved image current power ratio is 3.8, which is far from the target value of 2. Figure 16 shows what was achieved in the trade-off: the large α_0 weighting relative to the other α_i weights results in excellent band-pass behavior around the design frequency of 96 MHz: a wide band-pass is achieved where S_{11} is less than -30 dB from 92 to 101 MHz.

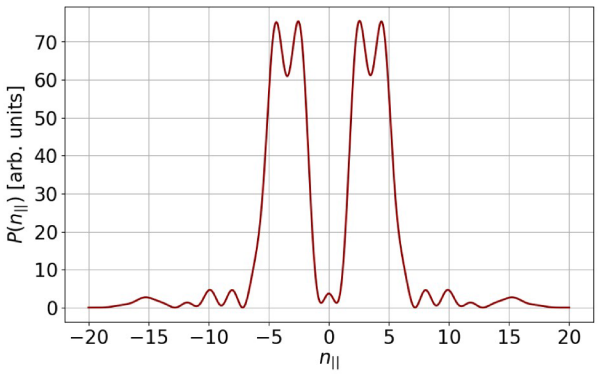

Figure 15: An example $P(n_{||})$ spectrum at 96 MHz for an antenna that weights band-pass behavior over spectrum control. Poor peak selectivity and large potential for coaxial modes are seen in this spectrum.

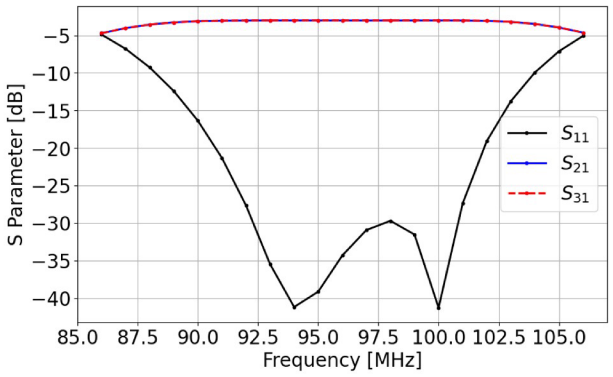

Figure 16: An antenna S_{11}, S_{21}, S_{31} only optimized for band-pass is shown. Less than -30 dB is achieved across a wide range of frequencies around the design frequency of 96 MHz, at the expense of spectrum control (see Figure 15).

The success of the passive straps in canceling the image currents on the antenna box is shown in Figure 17 by comparing the magnitude of the image currents with and without the passive straps. This comparison is slightly difficult to make in that simply removing the passive straps does perturb the antenna's $n_{||}$ spectrum, indicating the passive-strap-free version would not have been selected in the first place when designing. However, the comparison does show the effectiveness of the passive strap in canceling image currents on the antenna box (Figure 17 b) compared to simply terminating on a traveling wave end strap (Figure 17 a). Figure 17 c) shows a zoom-out of where the sections in a) and b) are located on the antenna. Note the shown antenna in c) includes the image current cancellation strap and thus corresponds to b): the coax port would need to be shifted left by one to match a). In a) without image current cancellation, the antenna box edge sees an elevated surface current magnitude, indicated by the black arrow, over b), where image current cancellation straps are used. The reduction is quantified by integrating the surface current magnitude on the small rectangular edge indicated by the black arrows in a) and b). The reduction is found to be 30 percent, with the achieved power ratio between the last traveling wave strap and the image current cancellation strap of 1.985, with a phase difference of 174 degrees between these two straps. Note the target power ratio $\mathrm{PR}_{\mathrm{target}}$ could be tweaked in future designs to achieve better image current reduction. Including α_3 and α_4 in the cost function in Equation 3 is a powerful design feature of the antenna here in that it gives the designer control over both the phase and power ratio of the passive straps. Although image currents have been reduced, quantification of image currents' impact on impurity production was left to future work, as explained later in the Discussion and Limitations section.

Parameter	Target	Achieved
S_{11} at 96 MHz	< -20 dB	-27.3 dB
Power ratio PR	2	1.985
$\Delta\Phi$	180°	174.9°
$n_{\|\|,\mathrm{peak}}$	5	4.51
$P(n_{\|\|}=0)/P_{\mathrm{max}}$	0	0.03

Table 2: Target and achieved values for the vacuum optimized antenna

The achievements of the vacuum optimization process for the center-fed traveling wave array antenna are summarized in Table 2, where design goals and achieved values are compared. Design trade-offs between these values were necessary in order to achieve an overall system that performed well on all metrics. The results in Table 2 demonstrate this design workflow robustly produces a satisfactory initial antenna design point for the flat version of the center-fed TWA for fast ion production. Next, the effect of a plasma load in front of the antenna is assessed to investigate how much deviation these values see when the load is no longer vacuum.

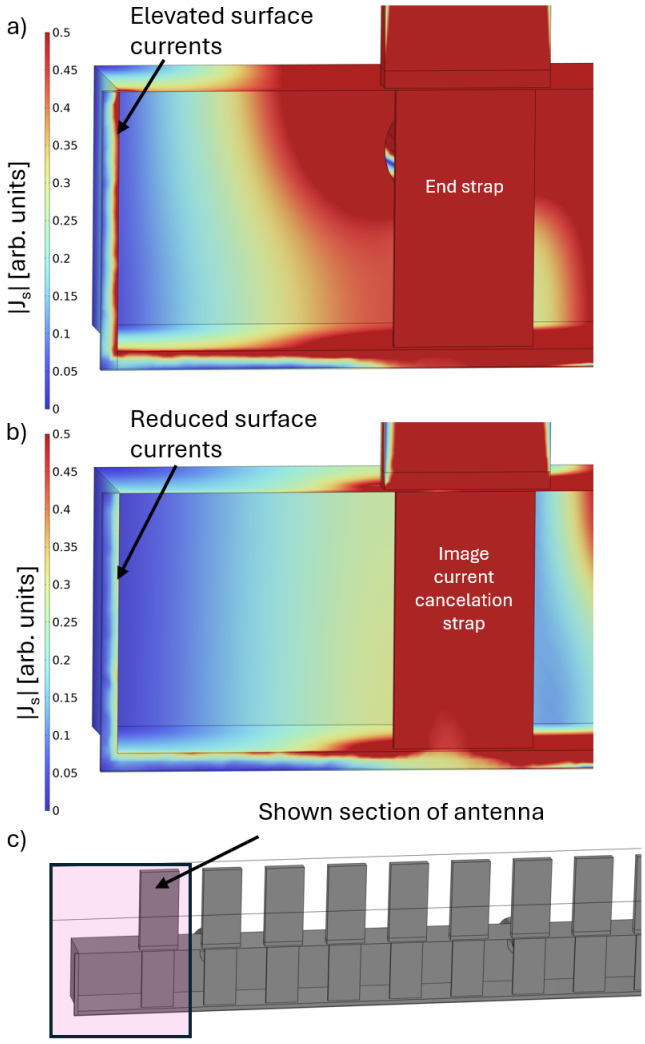

Figure 17: Comparison of image currents on antenna box edge (black arrow) when a) no image current cancellation straps are used, and b) when image current cancellation straps are used. A 30 percent reduction in surface current magnitude on the antenna box edge was achieved. Both antennas have the same number of non image current cancellation straps. Note the color range was maxed to 0.5 so the difference in current on the box edge between a) and b) is clearly visible.

4 Cold Plasma Influence on S_{11} and Power Spectrum

The antenna optimization in the COMSOL/Python workflow in Figure 12 was done in the vacuum load condition. This is typically cited in the literature [23] as acceptable for TWAs, which on a per-strap basis should be dominated by mutual coupling to the next strap rather than to the plasma load. This condition is achieved by a combination of operating the TWA as a low-Q resonator in a resonant ring circuit [23] or by adding more straps. However, the coupling to the plasma is crucial for meeting the main objective of coupling power to the plasma and damping it in the right place and on the correct species. It is shown in this section that a plasma load during optimization greatly helps the antenna perform well under fluctuations of the evanescent layer thickness about its expected thickness.

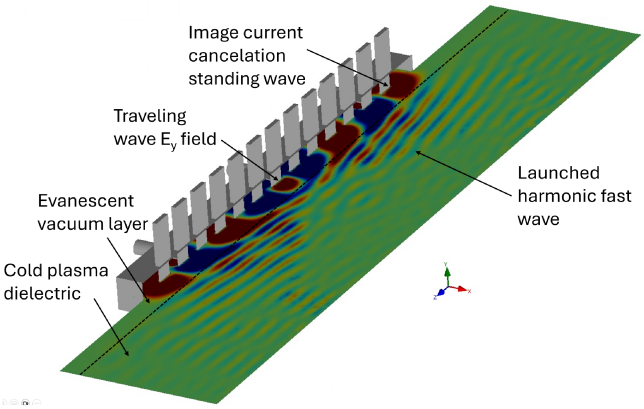

Figure 18: Petra-M model slice of the plasma showing the properties of the E_y field for the $d_{\text{vac}} = 10$ cm case, color units are arbitrary and are clipped to clearly see the launched fast wave in the plasma region.

To investigate the plasma load's effect on both the antenna power spectrum $P(n_{||})$ and reflection coefficient S_{11}, the Petra-M FEM multi-physics framework [39] [40] [41] [42] was used. Petra-M is a finite element tool that is designed for ease of use with the cold plasma dielectric tensor and tokamak equilibrium files, as well as being parallelized to run quickly on Perlmutter at NERSC [43], so it scales well to future more complicated antenna models and larger plasma volumes. For these reasons, Petra-M was selected over COMSOL for the plasma FEA modeling. Each Petra-M job was run at Perlmutter on 16 nodes, with 64 tasks each

allotted 64 CPU cores. Runs took less than 2 hours each with this configuration.

In this study, the electron density profile in Figure 3 is moved away from the plasma using an evanescent layer of varying thickness d_{vac} between the antenna face and the start of the density ramp to investigate how sensitive the antenna parameters are to the plasma load, which is a function of the evanescent length d_{vac} between the R-cutoff and the antenna face. The magnetic field is self-consistently shifted with the density profile as well. In this model, the magnetic field direction is assumed entirely in the $\hat{z}$ direction, with its magnitude dependence on x found by sampling the inboard mid-plane magnetic field magnitude profile of the high q_{min} discharge 147634 equilibrium.

A slice through the plasma volume for the $d_{\text{vac}} =$ 10 cm Petra-M case is shown in Figure 18 depicting the E_y component of the electric field (the component parallel to the strap current). The main regions of interest shown in the figure are the traveling wave within the antenna box, the evanescent region in front of the antenna face, and the launched high harmonic fast wave with $n_{||}$ approximately equal to ± 5. Non-physical damping is used to avoid reflection from the far plasma boundaries – which are non-physical perfect electric conductors – by defining a finite conductivity tuned to reduce the launched wave's magnitude by the time it reaches the far boundary. This artificial conductivity is kept constant throughout the variation of the evanescent layer thickness. In reality, the launched wave magnitude reduction seen in Figure 18 would match the extent of the rays shown in Figure 4: the magnitude would slowly decrease with electron damping and sharply decrease at the deuterium cyclotron resonances. The cold plasma dielectric tensor used in the Petra-M modeling does not capture these hot plasma damping effects.

The evanescent layer thickness d_{vac} was scanned between 2.5 cm and 17.5 cm in steps of 2.5 cm, and for each thickness, the E_y electric field on the face of the antenna box was Fourier transformed in the $\hat{z}$ direction to produce $P(n_{||})$ spectra. The spectrum was found to be robust to changes in the evanescent length from infinity (as the antenna was optimized in vacuum) to 5 cm, as shown in Figure 19, where each peak is normalized to the maximum of the individual spectra. At 2.5 cm, the spectrum peaks above and below the main peak increase in magnitude relative to the main peak, and the $n_{||} = 0$ component raises above its previous small magnitude. The larger $n_{||} = 0$ modes will excite unwanted coaxial modes, and the increased magnitudes near $n_{||} = 10$ will increase electron heating relative to ion heating as shown in Figure 5, correspondingly reducing SPA. The vacuum case in Figure 19 is in excellent agreement with the $P(n_{||})$ spectrum found by COMSOL in Figure 13.

For each evanescent layer thickness d_{vac}, the reflection coefficient S_{11} and transmission coefficients S_{21} and S_{31} were calculated at 96 MHz, and are displayed in Figure 20. At 17.5 cm, the reflection and transmission coefficients nearly match the vacuum case where the antenna was optimized. As d_{vac} is decreased, the reflection coefficient increases, passing -20 dB at 12 cm before rolling over and decreasing slightly again at 2.5 cm. Given that the transmission coefficient decreases continuously with d_{vac} into the low-d_{vac} region where S_{11} decreases again, conservation of energy indicates that the plasma load in this regime absorbs a high fraction of the power that is not reflected or transmitted at the ports. This regime may be undesirable despite the lower S_{11} as strong per-strap loading increases a TWA antenna's impedance match sensitivity [22].

Both the $P(n_{||})$ spectrum and the S parameters remain within the design boundaries specified for a wide range in d_{vac}, with $P(n_{||})$ being acceptable for $d_{\text{vac}} >$ 5 cm and S_{11} acceptable for $d_{\text{vac}} > 12$ cm. A vacuum design is suitable down to an evanescent layer of 12 cm. However, the distance between the high field side and the last closed flux surface of high q_{min} discharge 147634 is 5.5 cm, which with the current vacuum-optimized flat antenna design would fall within acceptable values for the $P(n_{||})$ spectrum, but not the reflection coefficient, which is above -20 dB for a 5.5 cm evanescent layer.

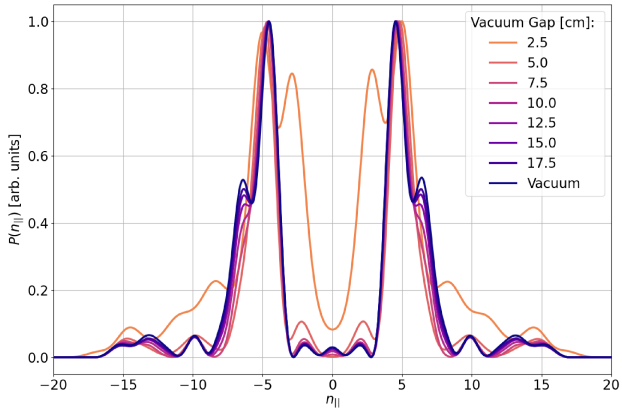

Figure 19: The power spectrum of the TWA under varying evanescent layer thicknesses between the antenna face and the plasma LCFS. The spectrum is resilient to plasma loading down to $d_{\text{vac}} = 5$ cm

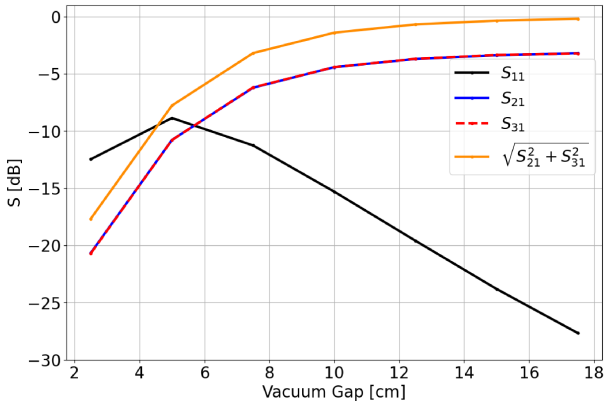

Figure 20: The S parameters response to varying evanescent layer thickness between the antenna face and the plasma LCFS at 96 MHz.

A strategy to remedy this issue is to optimize the antenna with the expected density profile as the dielectric in front of the antenna, instead of a vacuum. The above design workflow was run again with high q_{min} discharge 147634's 5.5 cm evanescent layer thickness to find a new set of capacitor values that produces an acceptable reflection coefficient around $d_{\text{vac}} = 5.5$ cm, while also trying to keep good power spectrum control and image current cancellation, strap power ratio, and phase. The same cost function coefficients α_i as used in Table 1 a) were found to work well, and produced an antenna with the capacitor values and achieved parameters at 96 MHz, $d_{\text{vac}} = 5.5$ cm, shown in Table 3.

a)

	C_p	C1	C2	C3	C4	C5	C6
l_{cap} [cm]	14.27	13.51	11.87	11.91	11.43	12.95	15.42

b)

Parameter	Target	Achieved
S_{11} at 96 MHz	< -20 dB	-35.5 dB
Power ratio PR	2	2.09
$\Delta\Phi$	180°	168°
$n_{\|\|,\text{peak}}$	5	4.58
$P(n_{\|\|}=0)/P_{\text{max}}$	0	0.04

Table 3: a) Capacitor lengths for a TWA optimized with a plasma load corresponding to $d_{\text{vac}} = 5.5$ cm. b) Target and achieved values.

The frequency response of the S parameters for this new plasma-optimized antenna is shown in Figure 21 with the $d_{\text{vac}} = 5.5$ cm load. The antenna now achieves a reflection coefficient of -35.5 dB at the design frequency, a drastic improvement over the -9 dB S_{11} value seen in Figure 20 for $d_{\text{vac}} = 5.5$ cm. The antenna reflection coefficient remains below -20 dB for roughly 1 MHz on either side of the design frequency.

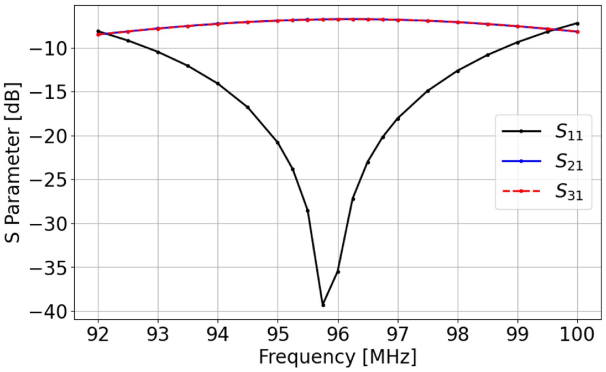

Figure 21: An antenna S_{11}, S_{21}, S_{31} optimized for 96 MHz and a plasma load with a 5.5 cm evanescent layer. Less than -20 dB is achieved for roughly 1 MHz on either side of the design frequency of 96 MHz.

The plasma-optimized antenna's reflection coefficient response to varying the evanescent layer thickness shows resilience to plasma density profile fluctuations

in Figure 22, remaining below -20 dB for 1 cm fluctuations on either side of the design $d_{\text{vac}} = 5.5$ cm. The antenna response here is much improved over the response for the vacuum-optimized antenna seen in Figure 20 for the realistic evanescent layer thickness of 5.5 cm. DIII-D HFS radial turbulent density fluctuations are being characterized for the HFS lower hybrid current drive system [44] but are not yet finished. The low field side has been characterized, with radial profile turbulent scales between 0.1 and 10 cm [45]. On C-Mod, it was reported that due to its more favorable magnetic curvature and higher field, the HFS saw factors of 5 to 10 reductions in the radial density turbulent fluctuation scale [46]. Assuming this factor holds for DIII-D, that puts DIII-D's maximum HFS fluctuations in the range of 1 to 2 cm, with much lower fluctuation sizes possible. This is very promising for this antenna's ±1 cm radial turbulent range tolerance. The actual expected turbulent scale will be known after the lower hybrid current drive HFS turbulence characterization on DIII-D is completed. Should the value be closer to ±2 cm, corresponding to -15 dB in the design here, active tuners could be added to the capacitors to maintain a good impedance match, but this is left to future work.

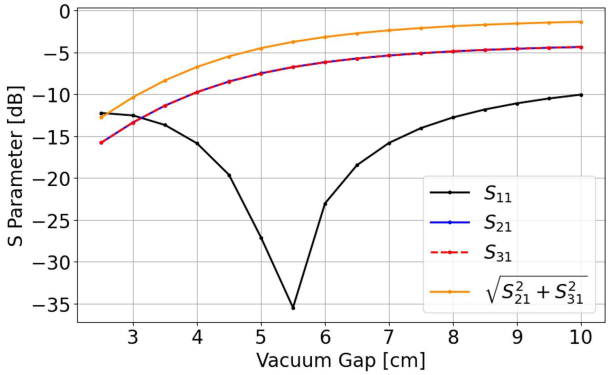

Figure 22: An antenna S_{11}, S_{21}, S_{31} and total transmission coefficient optimized for 96 MHz and a plasma load with a 5.5 cm evanescent layer. Shown is the response to change in d_{vac}. Less than -20 dB is achieved for roughly 1 cm evanescent gap fluctuations on either side of the design gap thickness of 5.5 cm, with below -10 dB performance across the range of gap thicknesses looked at.

The plasma-optimized antenna's power spectrum $P(n_{||})$ for various evanescent layer thicknesses is shown in Figure 23. The black dashed line is overlaid for easier visualization of the design spectrum at $d_{\text{vac}} = 5.5$ cm. The peak of the spectrum achieved was 4.58 for this case, with low coaxial mode potential due to $P(n_{||})$ being small at low $n_{||}$: $P(n_{||} = 0)/P_{\max} = 0.04$. However, the $n_{||} = 0$ mode does grow for off-design gap thicknesses larger than 5.5 cm, but not necessarily to a concerning level within the ±1 cm range where S_{11} remains below -20 dB. The spectrum performs well for variations of d_{vac} about 5.5 cm: down to 3.5 cm, below which the low $n_{||}$ magnitude begins to increase noticeably. Above 5.5 cm, two other peaks form at higher $n_{||}$. The larger of the two is at $n_{||} = \pm 6.7$, which would lead to some deleterious electron damping, however, Figure 5 still shows greater than 90 percent selectivity for ion damping at this $n_{||}$ which may still be acceptable. Of greater concern is the smaller new peak which forms at $n_{||} = \pm 12.6$, here electron damping would dominate and lower SPA would be achieved. The area under this smaller peak is small relative to the larger double peaks in the acceptable $n_{||}$ range, so this could potentially still be an acceptable performance at these larger evanescent gaps.

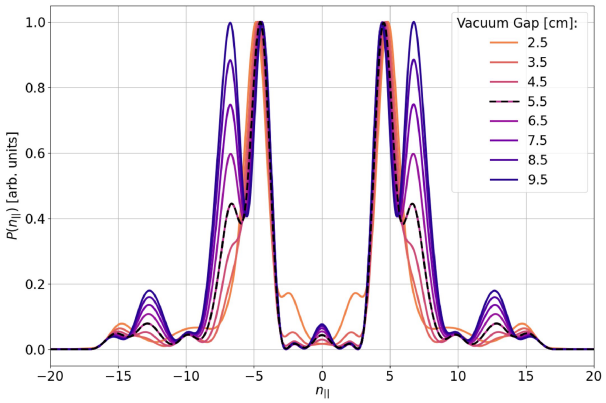

Figure 23: Power spectrum of the TWA optimized for a plasma load corresponding to $d_{\text{vac}} = 5.5$ cm under varying evanescent layer thicknesses between the antenna face and the plasma LCFS. The 5.5 cm spectrum is overlaid with a dashed black line for clarity, and shows good peaking near the $n_{||} = 5$ target, with small low $n_{||}$ features. The spectrum is now resilient to plasma loading down to $d_{\text{vac}} = 3.5$ cm and up to 7.5 cm before the secondary peak at larger $n_{||}$ begins to dominate.

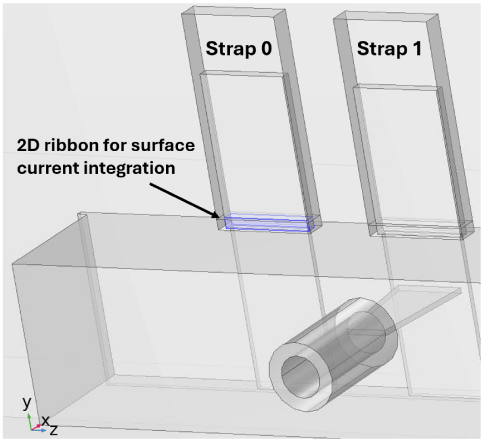

Figure 24: Ribbon-shaped 2D surface at capacitor entrance used for calculating the magnitude and phase of the y-directed current on each strap. The complex-valued j_y surface current is integrated on this ribbon, for each strap, over a range of frequencies.

Based on these results for the plasma-optimized TWA, should the HFS plasma density profile evanescent layer thickness fluctuate, the power spectrum should be relatively resilient to fluctuations of up to -2 cm to potentially +3 cm depending on if the high $n_{||}$ smaller peak's performance detriment due to electron damping dominates the double peak at large d_{vac}. More limiting is the S_{11} response (Figure 22), which remains below -20 dB for ± 1 cm about the design evanescent layer thickness. The quiescent nature of the HFS lends itself well to keeping the plasma density profile fluctuations in the range for which the TWA remains passively impedance-matched.

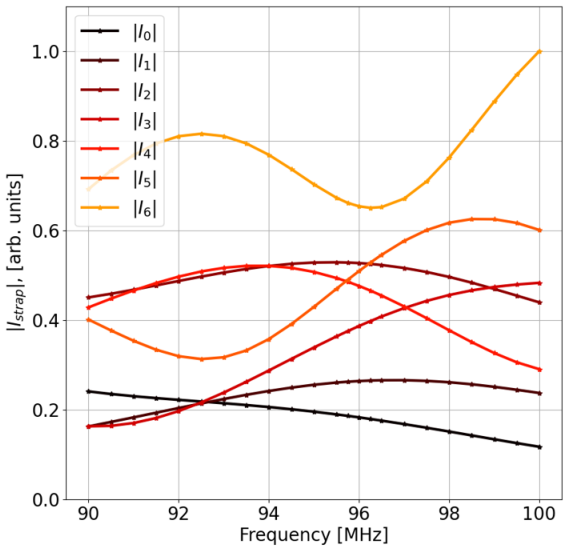

Figure 25: Current magnitude (arb. units) on the image current cancellation strap (strap 0) and straps 1 through 6 (see Figure 12, a) for numbering) for a range of frequencies from the FEA model. Note the ratio of the square of currents I_0 and I_1 at 96 MHz is 2.09, closely matching the target power ratio of 2.

The plasma-optimized antenna's strap current phases and relative magnitudes in the full finite element model were tabulated across the frequency range of 90 to 100 MHZ for a gap thickness of 5.5 cm to demonstrate how the image current cancellation straps and varied strap capacitance affect the design relative to a traditional TWA. The currents were calculated by integrating the j_y surface current on the ribbon shown in Figure 24, at the entrance of each capacitor box. In Figure 25, the magnitude of these currents is shown. Strap 0 is the image current cancellation strap, and straps 1 through 6 follow the numbering shown in Figure 12 a). Straps 7 through 11 are omitted from Figure 25 due to symmetry. Note that at 96 MHz, the ratio

of the square of currents I_0 and I_1 is 2.09, which was reported as the power ratio (PR) in Table 3 b), closely matching the Python scikit-rf model value of 2.006, indicating the Python RF model matches the full FEA model well.

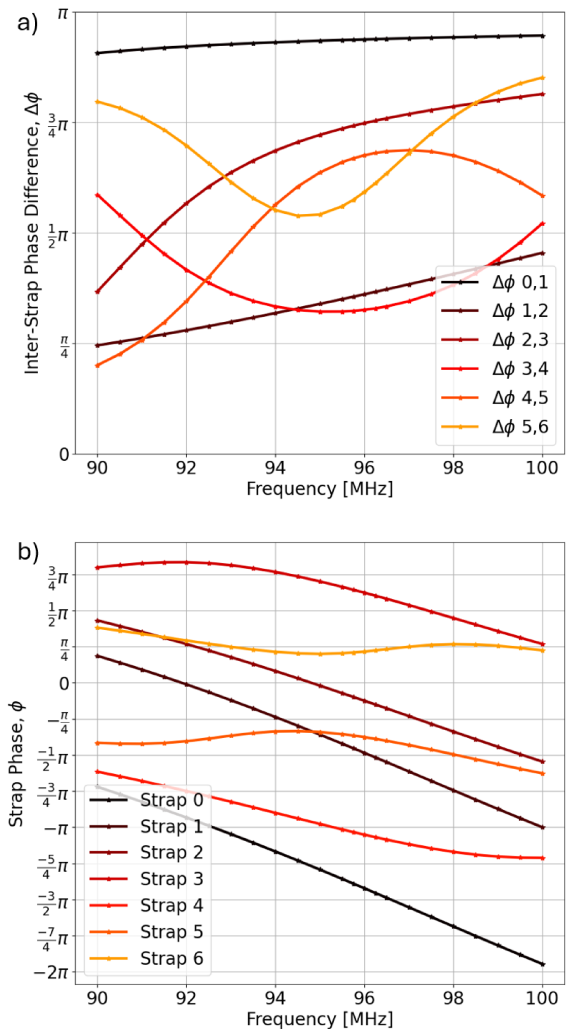

Figure 26: a) Phase difference between straps: $\Delta\phi$ i,j is the phase change between strap i and strap j. b) Phase of current on strap i, referenced to an arbitrary zero phase. Strap number corresponds to the numbering in Figure 12, with the exception of the image current cancellation strap labeled as Strap 0.

The inter-strap phase differences and absolute strap phases for the 90 to 100 MHz frequency range are shown in Figure 26 a) and b), respectively. Figure 26 a) shows the difference in the phases of the ribbon-integrated j_y surface current between straps: $\Delta\phi$ 0,1, for example, is the phase difference between strap 0 (the image current cancellation strap), and strap 1. Only half of the inter-strap phase differences are shown due to the antenna's symmetry about strap 6. Seen in a) is the nearly constant phase difference of roughly π between the image current cancellation strap 0 and the terminating line strap, strap 1, showing the image current cancellation method in terms of phase is well-maintained across frequencies in the pass band of Figure 21. For the other straps, the phase differences band $\pi/2 \pm$ roughly $\pi/4$, indicating that $\Delta\phi = \pi/2$ used in the calculation of inter-strap spacing d_s was reasonable. Figure 26 b) shows the absolute phase of the strap current, referenced to an arbitrary zero phase. Note that colors between Figure 26 a) do not exactly correspond to the colors used in Figure 26 b) and Figure 25 due to Figure 26 a) being the phase difference between adjacent straps.

The sensitivity of the plasma-optimized TWA's reflection coefficient to manufacturing tolerance differences in capacitor length were assessed in a similar manner to [20], where the lengths of the capacitors were individually varied randomly on a uniform distribution between +/- the selected tolerance. Tolerance variation perpendicular to the long dimension of the capacitors was not assessed. Here, ISO 2768 standard was assumed. For the capacitor lengths in Table 3, fine, medium, and coarse tolerance levels, corresponding to +/- 0.2, 0.5, and 1.2 mm, respectively, were used to investigate which tolerance level too drastically degraded the reflection coefficient's performance. This was accomplished through 4,000 variations of the capacitor lengths using the Python scikit-rf model, a task which would have been prohibitively computationally intensive for the FEA model. The spread of S_{11} values for three different choices of tolerance level about the nominal are shown in Figure 27. Note the black nominal curve uses points to indicate the frequencies looked at, and small discrepancies exist at more negative S_{11} between the black nominal curve here using the scikit-rf model, and Figure 21, where the same information is shown using the full FEA model.

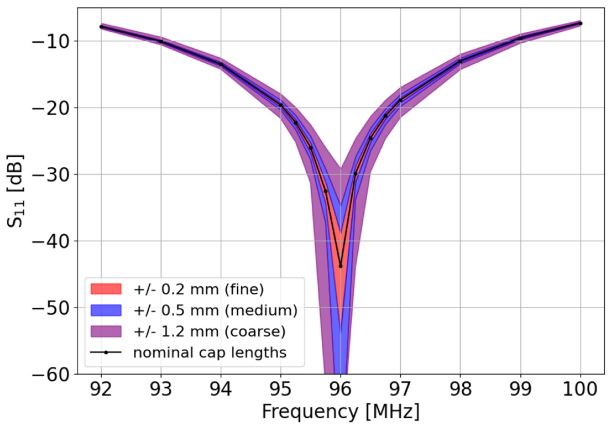

Figure 27: Plasma-loaded S_{11} response predicted by Python scikit-rf model for 4,000 random variations in the capacitor lengths. Black is nominal response, red is ISO 2768 fine tolerance level variations, blue is medium tolerance level variations, and purple is coarse tolerance level variations.

Figure 27 indicates that the ISO 2768 coarse tolerance level leads to the possibility of above -30 dB performance at the design frequency, as well as a noticeable decrease in the frequency range about the design frequency with sub -20 dB S_{11} performance. The medium tolerance level appears acceptable on both those metrics. Future work on a more finalized version of the antenna could also use this method to assess changes in performance due to thermal expansion, as was done in [20].

5 Discussion and Limitations

There are several immediate next-step physics modeling improvements that will be used to increase confidence in the antenna's ability to efficiently produce a sufficient population of fast particles with reactor-relevant parameters such as $V_{\mathrm{fast}}/V_{\mathrm{A}}$, $\beta_{\mathrm{EP}}/\beta_{\mathrm{th}}$, $\rho_{\mathrm{L,EP}}/a$, and fast particle distribution function. While the GENRAY/CQL3D workflow for fast scoping of SPA and preferential ion heating can still be used to explore parameter space, once target shots of interest are identified, like high q_{min} discharge 147634 presented in this work, higher-fidelity RF modeling tools should be used next on the identified shot. Uncertainty from GENRAY's ray approximation, while acceptable for the 5th to 8th harmonics used here, will be alleviated by moving to the full wave code AORSA [47], which can be paired to either CQL3D for comparison to the current workflow, or to either the Monte-Carlo orbit tracking code MCGO [48] [49] or CQL3D with finite orbit effects included via CQL3D-FOW [50]. Finite orbit effects smear out where the fast ions interact with the resonances in physical space due to the particle's drifts off of flux surfaces [51] and can lead to direct losses to the wall during a particle's wide excursions from a given flux surface, so SPA, ion to electron power partitioning, and the overall distribution function at a particular $\sqrt{\psi_{\mathrm{tor}}}$ will be affected, especially in the presence of fast RF ion tails. When paired with AORSA, MCGO or CQL3D-FOW should be able to produce accurate distribution functions of fast particles. With these distributions, the Alfven Eigenmode code Far3D [52] will be fed these distribution functions for outputting Alfven eigenmode activity. This AE activity can be used in addition to Figure 1 to compare to the activity expected in SPARC or ITER when all or many of the energetic particle parameters are matched between the burning experiment and the RF D-D experiment, further building confidence in the utility of an RF system for fast particle production on DD tokamaks.

The antenna design workflow presented in Sections 3 and 4 showed three examples of the workflow's ability to optimize TWA antennas, the first being optimized for good reflection coefficient, power spectrum control, and image current power ratio and phase in vacuum. The second was an example of only optimizing for S_{11} band-pass, and the third in Section 4 was optimized with Petra-M with a plasma load. The main takeaway here was that the best-performing optimization was the antenna optimized with the expected density profile as its dielectric – the vacuum-optimized antenna did not perform well enough on S_{11} down to the expected evanescent layer thickness. Therefore, we recommended using this method when proceeding to more detailed antenna designs.

In future work, the TWA design should graduate from the simple flat antenna approximation and use a curved antenna designed to fit on the high field side of the target device, along with the realistic full equilibrium magnetic field with both the toroidal and poloidal components present. Petra-M makes implementing this simple: EQDSK equilibria can be loaded in directly to the finite element model. Investigating field alignment of the TWA, and comparing the HFS and LFS for achieving this, would help show the advantage of the HFS's less aggressive incidence angle between the field and toroidal wall direction. Other changes to the antenna would be curving the capacitor plate edges to reduce internal fields, which was used in [20], and perhaps using more complicated capacitor plate shapes to maintain the design capacitance while also conforming to the geometric constraints of an installation.

The main motivation for adding the image current cancellation straps was to avoid impurity production. In this work, we have successfully reduced the image current magnitude, but future modeling will include Petra-M's RF rectified potential model [42] to explore impurity production propensity more carefully. Petra-M with RF rectification is capable of modeling RF sheath potentials and where they concentrate on the antenna. A full mapping of the rectified sheaths would help an antenna designer select a satisfactory image current power ratio and overall geometric configuration: RF sheath potential minimization via the image current cancellation straps would be a strong indication of the successful reduction of impurity production.

6 Conclusion and Next Steps

In this paper, a proof-of-principle design workflow for a flat traveling wave array antenna with several first-of-a-kind features has been demonstrated for the target application of generating large populations of fast ions efficiently to study reactor-relevant fast particle effects in existing tokamak devices. This is achieved via high harmonic heating which features good RF channeling to energetic particles at resonances around 8 times the cyclotron frequency. The TWA designed here features center-feeding, which produces a symmetric launched power spectrum (Figure 13) and makes adding image-current cancellation straps simpler, as well as allowing for good damping on co/counter zero-torque neutral beams. Image current cancellation straps are included to remove image currents on the antenna box to reduce impurity production, with future work left to demonstrate impurity reduction quantitatively.

GENRAY/CQL3D were used to scope neutral beam power, launched $n_{||}$, and RF power for good SPA and good ion power channeling in two potential DIII-D discharges. The conclusion here was high $q_{\min}$ discharge 147634 made an excellent candidate shot for 96 MHz 8th harmonic heating, with 5 MW of NBI power paired with 700 kW of launched RF power and a peak $n_{||}$ of 5 achieving an SPA of nearly 1 with 99.85% of the RF power channeled to the ions. Even higher ion channeling was seen for $n_{||} < 5$, but this was not pursued in order to avoid the excitation of coaxial modes and an excessively large antenna footprint. In Figure 8, the scheme succeeds in producing elevated populations of fast particles out to reactor relevant values of $V_{\text{fast}}/V_{\text{A}}$ and separately $\rho_{\text{L,EP}}/a$. Recommendations were given for how to design an experiment to match these parameters simultaneously better by looking at Super H-mode shot 201991. This successfully moved the SPARC and ITER $V_{\text{fast}}/V_{\text{A}}$ and $\rho_{\text{L,EP}}/a$ values into the non-Maxwellian portion of the distribution, and produced an elevated high-energy tail over high $q_{\min}$ discharge 147634. This came at the expense of reduced SPA and ion selectivity due to the higher density plasma reducing neutral beam penetration, and the larger spacing between cyclotron harmonics reducing the number of sites for fast ion heating present over the first pass of the wave. The reduced RF performance may still be acceptable, but strategies to improve it were given, including using higher beam power if the co/counter beam balance constraint was relaxed, or if operation at a lower $n_{||} = \pm 3$ was acceptable.

An RF-optimization scheme inspired by previous

work [20] was expanded on, building out a cost function optimizing for antenna reflection coefficient, peak $P(n_{||})$ location, low coaxial mode excitation and controllable power ratio and phase between the new image current cancellation straps and the traveling wave termination straps. A hybrid COMSOL-Python and Petra-M-Python tool was built to quickly scan capacitor values for the minimization of the cost function, which was achieved using the global optimization algorithm *differential_evolution*. Three example antennas were shown in Sections 3 and 4 to showcase the versatility of the design tool. The first was optimized with COMSOL in vacuum, the second for wide S_{11} bandpass alone, and the third with a realistic plasma density profile using Petra-M. The inclusion of the image current cancellation straps resulted in a 30% reduction in surface current magnitude on the antenna box and could be further optimized by changing the power ratio target (2 was chosen arbitrarily for proof of principle here).

The best-performing optimization across all metrics of performance was the antenna optimized with Petra-M using a realistic density profile for the desired shot as the dielectric load. It is recommended to use this method as future more detailed antenna designs are iterated on.

Avenues for future work were presented in the Discussion and Limitations section, and include more detailed RF physics modeling codes to capture missing physics, Alven eigenmode codes to investigate AE activity produced by a given workflow-generated distribution function, and further finite element modeling including realistic geometries, magnetic equilibria, and the inclusion of sheath potential effects.

Acknowledgments

The PSFC work was funded by the US Department of Energy under Contract Number DE-SC0014264. The PPPL work was supported by the US Department of Energy under Contract Number DE-AC02-09CH1146. This material is based upon work supported by the U.S. Department of Energy, Office of Science, Office of Advanced Scientific Computing Research and Office of Fusion Energy Sciences, Scientific Discovery through Advanced Computing (SciDAC) program under Award Number DE-SC0024369. This research used resources of the National Energy Research Scientific Computing Center, a DOE Office of Science User Facility supported by the Office of Science of the U.S. Department of Energy under Contract No. DE-AC02-05CH11231 using NERSC award FES-ERCAP0027700. We would like to thank Grant Rutherford, Yuri Petrov, and Raymond Diab for their support during the setup of several of the codes used, and Riccardo Ragona for helpful discussions of TWA antennas. The authors declare no conflicts of interest.

References

[1] ITER Physics Basis Editors, *et al.*, "Overview and Summary ITER Physics Basis," *Nuclear Fusion*, vol. 39, no. 2137, 1999.

[2] P. Rodriguez-Fernandez *et al.*, "Overview of the SPARC physics basis towards the exploration of burning-plasma regimes in highfield, compact tokamaks," *Nuclear Fusion*, vol. 62, no. 042003, 2022.

[3] J. Ongena *et al.*, "Recent advances in physics and technology of ion cyclotron resonance heating in view of future fusion reactors," *Plasma Physics and Controlled Fusion*, vol. 59, no. 054002, 2017.

[4] D. Hill *et al.*, "White paper: Realize the full potential of DIII-D to advance development of cost-effective fusion power plants." Private communication with Dr. Michael Van Zeeland at General Atomics, Dec 2024.

[5] W. W. Heidbrink, "Basic physics of Alfvén instabilities driven by energetic particles in toroidally confined plasmasa," *Physics of Plasmas*, vol. 15, no. 055501, 2008.

[6] W. W. Heidbrink and R. B. White, "Mechanisms of energetic-particle transport in magnetically confined plasmas," *Physics of Plasmas*, vol. 27, no. 030901, 2020.

[7] B. N. Sorbom *et al.*, "ARC: A compact, high-field, fusion nuclear science facility and demonstration power plant with demountable magnets," *Fusion Engineering and Design*, vol. 100, pp. 378–405, 2015.

[8] R. Kembleton *et al.*, "EU-DEMO design space exploration and design drivers," *Fusion Engineering and Design*, vol. 178, no. 113080, 2022.

[9] M. Ono, "High harmonic fast waves in high beta plasmas," *Physics of Plasmas*, vol. 2, no. 11, 1995.

[10] LeBlanc *et al.*, "Recent developments in high-harmonic fast wave physics in NSTX," in *AIP Conference Proceedings*, no. 1187, 2009.

[11] G. Taylor, "Advances in high-harmonic fast wave physics in the National Spherical Torus Experiment," *Physics of Plasmas*, vol. 17, no. 056114, 2010.

[12] J. Menard, "Overview of the physics and engineering design of NSTX upgrade," *Nuclear Fusion*, vol. 52, no. 083015, 2012.

[13] N. Bertelli, "Modeling of high harmonic fast wave scenarios for NSTX Upgrade," *Nuclear Fusion*, vol. 59, no. 086006, 2019.

[14] M. Choi, V. S. Chan, R. I. Pinsker, S. C. Chiu, and W. W. Heidbrink, "Monte carlo orbit/full-wave simulation of ion cyclotron resonance frequency wave damping on resonant ions in tokamaks," *Physics of Plasmas*, vol. 12, no. 072505, 2005.

[15] T. Stix, *Waves in Plasmas*. Springer Science and Business Media, 1992.

[16] A. Smirnov and R. Harvey, "Calculations of the current drive in DIII-D with the GENRAY ray tracing code," *Bull. Am. Phys. Soc*, vol. 40, no. 1837, p. 35, 1995.

[17] R. Harvey and M. McCoy, "The CQL3D Fokker-Planck code," in *Proceedings of the IAEA Technical Committee Meeting on Simulation and Modeling of Thermonuclear Plasmas*, pp. 489–526, 1992.

[18] Chiu *et al.*, "Study of the slow-wave structure as an ICRF launcher," *Nuclear Fusion*, vol. 24, no. 6, p. 717, 1984.

[19] C. P. Moeller, R. Pinsker, *et al.*, "Combline antennas for launching traveling fast waves," *American Institute of Physics*, vol. 289, pp. 55–58, 1994.

[20] R. Ragona *et al.*, "RF network analysis of the WEST TWA mock-up in TITAN," *Fusion Engineering and Design*, vol. 168, no. 112615, 2021.

[21] R. Ragona, A. Messiaen, *et al.*, "Traveling wave array for DEMO with proof of principle on WEST," *Fusion Engineering and Design*, vol. 146, pp. 854–857, 2019.

[22] R. Ragona and A. Messiaen, "Conceptual study of an ICRH traveling-wave antenna system for low-coupling conditions as expected in DEMO," *Nuclear Fusion*, vol. 56, no. 076009, 2016.

[23] R. Ragona and A. Messiaen, "Multi-section traveling wave antenna for heating of large machines as DEMO," *Fusion Engineering and Design*, vol. 123, pp. 232–235, 2017.

[24] X. Litaudon *et al.*, "Physics and technology in the ion-cyclotron range of frequency on Tore Supra and TITAN test facility: implication for ITER," *Nuclear Fusion*, vol. 53, no. 083012, 2013.

[25] R. Ragona, A. Messiaen, *et al.*, "Status of the WEST traveling wave array antenna design and results from high-power mock-up," *Nuclear Fusion*, vol. 62, no. 026046, 2022.

[26] Ongena *et al.*, "Conceptual study of an ICRH system for T-15MD using traveling wave antenna

(TWA) sections," *Fusion Engineering and Design*, vol. 146, pp. 787–791, 2019.

[27] R. Prater *et al.*, "Application of very high harmonic fast waves for off-axis current drive in the DIII-D and FNSF-AT tokamaks," *Nuclear Fusion*, vol. 54, no. 083024, 1914.

[28] R. I. Pinkser *et al.*, "Experiments on helicons in DIII-D—investigation of the physics of a reactor-relevant non-inductive current drive technology," *Nuclear Fusion*, vol. 58, no. 106007, 2018.

[29] B. Grierson *et al.*, "Testing the DIII-D co/counter off-axis neutral beam injected power and ability to balance injected torque," *Nuclear Fusion*, vol. 61, no. 116049, 2021.

[30] V. Bobkov *et al.*, "Impact of ICRF on the scrape-off layer and on plasma-wall interactions: From present experiments to fusion reactor," *Nuclear Materials and Energy*, vol. 18, pp. 131–140, 2019.

[31] P. Bonoli *et al.*, "High field side lower hybrid wave launch for steady-state plasma sustainment," *Nuclear Fusion*, vol. 58, no. 126032, 2018.

[32] N. Smick, B. LaBombard, and I. Hutchinson, "Transport and drift-driven plasma flow components in the alcator c-mod boundary plasma," *Nuclear Fusion*, vol. 53, no. 023001, 2013.

[33] V. Compernolle *et al.*, "The high-power helicon program at DIII-D: gearing up for first experiments," *Nuclear Fusion*, vol. 61, no. 116034, 2021.

[34] M. Greenwald, "Density limits in toroidal plasmas," *Plasma Physics and Controlled Fusion*, vol. 44, pp. 27–80, 2002.

[35] "COMSOL Multiphysics." https://www.comsol.com/.

[36] A. Arsenovic *et al.*, "scikit-rf: An open source python package for microwave network creation, analysis, and calibration," *IEEE Microwave Magazine*, vol. 23, 2022.

[37] G. Wallace, *Behavior of Lower Hybrid Waves in the Scrape Off Layer of a Diverted Tokamak*. PhD thesis, Massachusetts Institute of Technology, 2010.

[38] R. Storn and K. Price, "Differential evolution – a simple and efficient heuristic for global optimization over continuous spaces," *Journal of Global Optimization*, vol. 11, pp. 341–359, 1997.

[39] S. Shiraiwa, J. C. Wright, P. T. Bonoli, T. Kolev, and M. Stowell, "RF wave simulation for cold edge plasmas using the MFEM library," in *AEPJ Web of Conferences*, vol. 157, 2017.

[40] N. Bertelli, S. Shiraiwa, and M. Ono, "3D full wave fast wave modeling with realistic HHFW antenna geometry and SOL plasma in NSTX-U," *Nuclear Fusion*, vol. 62, no. 126046, 2022.

[41] N. Bertelli, S. Shiraiwa, W. Helou, D. Milanesio, and W. Tierens, "Benchmark between antenna code TOPICA, RAPLICASOL and Petra-M for the ICRH ITER antenna," *AIP Conference Proceedings*, no. 060006, 2023.

[42] S. Shiraiwa, N. Bertelli, P. Bonoli, *et al.*, "Verification/validation and physics model extension in high fidelity 3D RF full wave simulations on Petra-M," *AIP Conference Proceedings*, no. 030007, 2023.

[43] "NERSC supercomputing cluster." https://www.nersc.gov/users/accounts/user-accounts/acknowledge-nersc/.

[44] E. Leppink, "Simulation-based inference of high field side scrape-off layer filament characteristics using profile reflectometry." Conference Talk at 66th Annual Meeting of the APS Division of Plasma Physics, 2024.

[45] J. Boedo, "Edge turbulence and SOL transport in tokamaks," *Journal of Nuclear Materials*, vol. 390-391, pp. 29–37, 2009.

[46] J. L. Terry *et al.*, "Observations of the turbulence in the scrape-off-layer of Alcator C-Mod and comparisons with simulation," *Physics of Plasmas*, vol. 10, no. 5, pp. 1739–1747, 2003.

[47] E. Jaeger *et al.*, "All-orders spectral calculation of radiofrequency heating in two-dimensional toroidal plasmas," *Physics of Plasmas*, vol. 8, no. 157383, 2001.

[48] R. Harvey and Y. V. Petrov, "A comparison of RF heating calculated with the CQL3D Fokker-Planck solver and with a Monte-Carlo code," in *AIP Conference Proceedings*, no. 2254, 2020.

[49] Y. V. Petrov, R. W. Harvey, N. Bertelli, and M. Podestà, "Modeling of ion losses in an NSTX/HHFW scenario with the RF monte-carlo code MCGO coupled to TORIC," in *AIP Conference Proceedings*, no. 2984, 2023.

[50] Y. V. Petrov and R. W. Harvey, "A fully-neoclassical finite-orbit-width version of the CQL3D Fokker–Planck code," *Plasma Physics and Controlled Fusion*, vol. 58, no. 115001, 2016.

[51] M. Choi *et al.*, "Iterated finite-orbit monte carlo simulations with full-wave fields for modeling tokamak ion cyclotron resonance frequency wave heating experiments," *Physics of Plasmas*, vol. 17, no. 056102, 2010.

[52] J. Varela *et al.*, "Analysis of Alfven eigenmodes destabilization by energetic particles in large helical device using a Landau-closure model," *Nuclear Fusion*, vol. 57, no. 046018, 2017.